TRENDS IN SCIENCES 2025; 22(12): 11063
https://doi.org/10.48048/tis.2025.11063
RESEARCH ARTICLE

New AIE+ESIPT β-Naphthol Azine-based Chemosensor of Cu^{2+} ions, An Experimental and In Silico Analysis

Dessy Eka Putri Romadhon, Rizka Permata, Juliandri, Dadan Sumiarsa, Rani Maharani, Ace Tatang Hidayat and Jamaludin Al-Anshori*

Department of Chemistry, Faculty of Mathematics and Natural Sciences, Universitas Padjadjaran, West Java 45363, Indonesia

(*Corresponding author's e-mail: jamaludin.al.anshori@unpad.ac.id)

Received: 25 June 2025, Revised: 12 July 2025, Accepted: 22 July 2025, Published: 30 September 2025

Abstract

A straightforward imine condensation reaction successfully yielded a novel and promising fluorescent chemosensor for Cu^{2+} ions, derived from the β-naphthol azine moiety, with a 26% chemical yield of a yellowish solid. Subsequent spectroscopic analyses employing FTIR, ToF-HRMS, ^{1}H-NMR, and ^{13}C-NMR elucidated the structure as 1-((((4-bromothiophen-2-yl)methylene)hydrazono)methyl)naphthalen-2-ol (**1**). The photophysical properties of the compound were characterized by a maximum UV/Visible absorption in a DMF:H_2O (1:9, *v/v*, c: 1.0×10^{-5} mol dm^{-3}) at 414 nm (ε: 6.80×10^{3} mol^{-1} dm^{3} cm^{-1}) and emission at 565 nm (λ_{ex} 360 nm), exhibiting a significant Stokes shift of 151 nm. Furthermore, at elevated concentrations (1.0×10^{-4} mol dm^{-3}), the compound exhibited aggregation-induced emission (AIE) in response to increased water content in the organic solvent mixtures. The compound functioned as a moderately reversible on-off chemosensor for Cu^{2+}, demonstrating a 1:1 molar ratio binding mode and a 96% quenching efficiency ((ϕ_{em} of **1** = 0.252 ± 0.030; 1+Cu^{2+} = 0.012 ± 0.004), as determined by a sensing experiment of **1** against various cations in DMF:H_2O (1:9, *v/v*). The Limits of Detection (LoD) and Quantification (LoQ) for **1** against Cu^{2+} ions were identified as 0.606 µM and 1.836 µM, respectively. Additionally, computational studies utilizing DFT and TD-DFT, accompanied by frontier molecular orbital (FMO) analysis, confirmed the presence of excited-state intramolecular proton transfer (ESIPT) in **1**, which was further inhibited upon chelation with Cu^{2+} ions.

Keywords: AIE, Chemosensor, DFT, ESIPT, Fluorescence, β-naphthol

Introduction

Copper (Cu^{2+}) is the third most abundant heavy metal after Fe^{3+} and Zn^{2+} [1]. Therefore, due to its widespread use, Cu^{2+} is a significant metal pollutant among all metal ions [2]. As a cofactor in about 20 enzymes (metalloenzymes), copper, in particular, is a vital micronutrient and plays a considerable role in biological processes. Take cytochrome C oxidase, tyrosinase, and superoxide dismutase, for instance [3-5]. An appropriate level of copper is also necessary for several other biological processes, including the creation of red blood cells and bone [6]. However, elevated concentrations of Cu^{2+} lead to oxidative stress and conditions linked to neurodegenerative illnesses such as Alzheimer's [7], Wilson's [8], and Menke's [9]. Low levels, however, can impact bone and brain development, as well as the immune system [10]. Furthermore, chronic exposure to elevated Cu^{2+} levels has been linked to renal and liver damage. When released into the environment in uncontrolled quantities, agricultural and industrial copper waste becomes a significant environmental contaminant [11-13]. As a result, research on Cu^{2+} detection holds considerable potential.

Numerous sensor innovations have been made to identify transitions of heavy metal ions in biological and environmental systems [14-16]. Research mainly

focuses on developing probes for colorimetric imaging and/or fluorescence systems that are selective for heavy metal ions [14,17]. Because of their low detection rate, high selectivity and sensitivity, and simplicity of use [18-21], these fluorescence probes become a new promising technique for metal ions among the well-established analysis methods of Cu^{2+} such as volumetric [22], spectrophotometric UV/Vis [23], atomic absorption spectrometry (AAS) [24,25], inductively coupled plasma mass spectrometry (ICP-MS) [26], potentiometric [27,28], voltammetry [29], X-Ray Fluorescence (XRF) [30-34], laser-induced breakdown spectroscopy (LIBS) [35,36], and CdTe quantum dots (QDs) [37]. Nevertheless, most Cu^{2+} sensors suffered interference from competing cations such as Zn^{2+}, Hg^{2+}, Pb^{2+}, Fe^{3+}, and Ag^{+} [38-40]. Consequently, considerable interest remained in developing highly selective fluorescence probes for copper ions.

Because their structural, spectral, and chemical properties are easily modified and rely on the structural characteristics of the ligands, chelated Schiff base fluorescent molecules are of great interest [28,41]. Specifically, the stability of the complex, achieved through the suppression of azomethine group isomerization, has a considerable effect on the fluorescence [42]. Another class of Schiff base groups that has the potential to improve a chemosensor's stiffness and selectivity is azine, an extended Schiff base moiety [43,44]. Furthermore, by modifying the Schiff base moiety in this way, the sensor can undergo an ESIPT or AIE mechanism [45], for some cases, could be AIE+ESIPT [46-48], which enhances its photophysical characteristics and yields benefits like various wavelength emissions and significant Stokes shifts because of enol-keto tautomerization [49-50].

ESIPT is generally reported as a fast-occurring mechanism with velocities ranging from fractions of a picosecond to tens of picoseconds [42]. To verify the ESIPT process instead, a DFT/TD-DFT computational calculation is frequently employed [49,51-55]. Therefore, adding the azine moiety, which functions as a hydrogen acceptor and enhances ligand stability, is anticipated to improve both the ESIPT process and the sensor's fluorescence in response to a Cu^{2+} metal ion. In addition, a restriction on intramolecular rotation (RIR) of an azine's rotatable nitrogen single bond (=N-N=) might be diminished and promote an AIE mechanism [56,57].

Here, we developed a novel and intriguing Cu^{2+} ion chemosensor in an aqueous system, demonstrating an AIE-ESIPT mechanism. Furthermore, an in-silico study investigated the sensor's behavior before and after ion chelation.

Materials and methods

The reagents and solvents employed were of synthetic and analytical grade, obtained from Sigma-Aldrich and Merck. Before use, all laboratory glassware items were oven-dried. Agilent 500 MHz and 125 MHz spectrometers were used to collect the ^{1}H- and ^{13}C-NMR spectra, which were recorded in $CDCl_3$. The (major) solvent's remnant peak served as a reference for the NMR signals. A Shimadzu 8,400 UV/Vis spectrometer was used to evaluate the molar absorptivity and UV/visible absorption spectra in matched 1.0 cm quartz cells. The spectra were captured using data at 0.1 nm intervals. At 25 °C, emission spectra were acquired in a quartz fluorescence cuvette with a 1.0 cm path length using an automated Agilent G9800A Cary Eclipse spectrometer. The slits for excitation and emission were set to 2.5 nm and 20 nm, respectively, while the scanning speed was 600 nm min^{-1}. The average of the resultant spectra was at least 3 times that of the observations from the sample.

Infrared spectra were recorded using a potassium bromide (KBr) pellet on a Perkin-Elmer FTIR. In both positive and negative ion modes, relative masses were determined using a Waters High-Resolution Time-of-Flight Mass Spectrometer (Lockspray/HR-TOF-MS). The uncorrected melting points were obtained from MP55 electrothermal equipment with a capillary tube. The DLS particle size distribution analysis was performed using the Horiba nanoPartica SZ-100V2 Series. DFT and TD-DFT computations [58,59] were run on a PC equipped with an Intel®Xeon (R) CPU E5-2650 v2@2.60 GHz × 32 processor, 16 GB of RAM, an SSD PCIe hard drive, and a Zotac GeForce GTX 1080TI AMP EXT CORE VGA. The calculation was performed using the Gaussian 09 program licensed to our university [49] with the B3LYP level of theory and a 6-311+G(d,p) basis set [14]. The Integral Equation Formalism Variant Polarizable Continuum Model (IEFPCM) was used in the computations to account for the solvent effect of DMF/H_2O, thereby attaining the actual

conditions of the tests [49, 60-65]. Parameters including structural geometry, the infrared and UV/Vis spectrum, and the energy bandgap of HOMO–LUMO were all determined to analyze the mechanism of interaction and the occurrence of the enol-keto upon an ESIPT process [49].

Synthesis of 1-((((4-bromothiophen-2-yl)methylene)hydrazineylidene)methyl)naphthalen-2-ol (1)

Compound **1** was synthesized using the analog method described in the publication by Al-Anshori *et al.* [51]. A 25 mL single-neck round-bottom flask (RBF) was filled with 2-hydroxy-1-naphthaldehyde **4** (0.25 g, 1.45 mmol, 1 eq) and hydrazine monohydrate 98% **5** (0.36 mL, 7.26 mmol, 5 eq), which were then dissolved in 10 mL of methanol. Following 2 h of stirring at room temperature, the reaction progressed with TLC (silica gel GF_{254}, eluent of *n*-hexane:ethylacetate (8:2, *v*/*v*)). After the solvent evaporated under vacuum, a crude yellowish solid of **2** was obtained, which was then used for the subsequent process without any further purification. A crude of 1-(hydrazineylidenemethyl)naphthalen-2-ol **2** (0.47 g, 2.52 mmol, 1 eq) was added into a 25 mL of three-neck rbf and dissolved in 15 mL of ethanol. Subsequently, 4-bromothiophene-2-carboxaldehyde **3** (0.53 g, 2.78 mmol, 1.1 eq) was added to the solution and refluxed for 2 h. The resulting precipitated product was then filtered and recrystallized from a mixture of acetone and ethyl acetate to yield a yellowish, pure solid (26%, 0.24 g). Upon a TLC (silica gel GF_{254}) using a mixture of *n*-hexane:ethylacetate (10:1, *v*/*v*) eluents, purity **1** was verified. M.P. 212-214 °C. IR Spectra (KBr) $\bar{\nu}$/cm^{-1}: 3,106 (C-H sp^2, sharp), 1,602 (C=N, medium), 1,534 (C=C aryl, strong), 1,299 (C-O β-naphthol, strong). UV/Visible spectra in DMF (1.0×10^{-5} mol dm^{-3}), λ_{max} /nm (ε/mol^{-1} dm^3 cm^{-1}): 338 (1.49×10^4), 395 (1.93×10^4); in DMF:H_2O (1:9, *v*/*v*, 1.0×10^{-5} mol dm^{-3}), λ_{max}/nm (ε/mol^{-1} dm^3 cm^{-1}): 414 (6.80×10^3); Emission spectra in DMF:H_2O (1:9, *v*/*v*, 1.0×10^{-5} mol dm^{-3}), λ_{ex} /nm, λ_{em} /nm and $\Delta\lambda$/nm: 360, 565 and 151, respectively. ^{1}H-NMR (500 MHz, $CDCl_3$) δ/ppm; 13.14 (1H, s, H-12), 9.68 (1H, s, H-15), 8.73 (1H, s, H-11), 8.17 (1H, d, *J* = 8.5 Hz, H-1), 7.88 (1H, d, *J* = 9.0 Hz, H-10), 7.81 (1H, d, *J* = 7.8 Hz, H-4), 7.42 (1H, t, H-5), 7.24 (1H, d, *J* = 9.0 Hz, H-21), 7.57 (1H, m, H-6), 7.41 (1H, s, H-19), and 7.39 (1H, s, H-9); ^{13}C-NMR (125 MHz, $CDCl_3$) δ/ppm; 108.18, 110.80, 119.16, 120.11, 123.80, 127.41, 127.99, 128.17, 129.19, 132.75, 134.33, 134.96, 139.53, 153.38, 161.33, and 162.09. ToF-HRMS (ES^+) *m*/*z*: $[M+H]^+$ calculated for $[C_{16}H_{11}BrN_2OS\text{-}H]^+$: 358.9848, found: 358.9851.

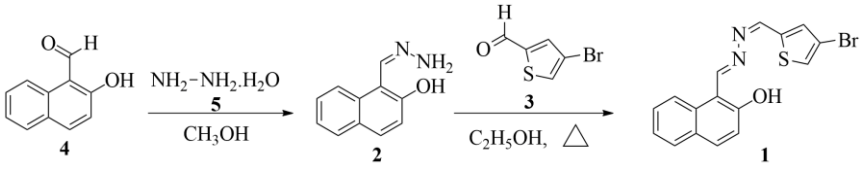

Scheme 1 Synthesis of compound **1**.

Chemosensory assay of compound 1 against numerous cations

The assay followed the standard protocol of Al Anshori *et al.* [51]. A 5 mL of the volumetric flask was used to separately prepare a stock solution (1.0×10^{-3} mol dm^{-3}) of compund **1** in DMF, and different cations obtained from sulphate salt (K^+, Li^+, Mg^{2+}, Fe^{2+}, Ni^{2+}, Cu^{2+}, Al^{3+}, Zn^{2+}) and nitrate salt (Co^{2+}, Cd^{2+}, Hg^{2+}, Pb^{2+}, Ag^+, and Cr^{3+}) in distilled water (0.18 mS/cm). Then, the solution of stock compound **1** and each cation were blended in the ratios of 9:1 to 1:9, with a final ratio of DMF:H_2O of 1:9 (*v*/*v*) and a total concentration of 1.0×10^{-4} mol dm^{-3}. Next, each combination was visualized over 365 nm UV light, accompanied by UV/Vis and fluorescence spectra at λ_{ex} 360 nm measurements. Job's plot experiment [66] calculated the ligand's binding ratio towards Cu^{2+}. Meanwhile, the selectivity experiment was accomplished by mixing a stock solution (1.0×10^{-3} mol dm^{-3}) of compound **1** in DMF with a cation solution (1.0×10^{-3} mol dm^{-3}), which exposed the most remarkable positive response at a specific stoichiometry acquired from the chemosensory assay. Subsequently, a further equivalent of each competitive cation was independently contaminated to

the mixture, resulting in a final ratio of DMF:H_2O of 1:9 (*v*/*v*) and a total concentration of 1.0×10^{-4} mol dm^{-3}. Next, the fluorescence spectra of each combination were captured at λ_{ex} 360 nm and λ_{em} 565 nm.

A titration of compound **1** (5.0×10^{-5} mol dm^{-3}) with the Cu^{2+} metal ion (1.0×10^{-5} mol dm^{-3}) in DMF:H_2O (1:9, *v*/*v*) was carried out using a spectrophotometric UV/Vis to track the change in their absorbances to find the association constant. The complex stability constant was computed using a Benesi-Hildebrand equation [67,68]. Following a spectrofluorometry measurement of a comparable titration procedure of compound **1** in DMF:H_2O (1:9, *v*/*v*, 1.0×10^{-4} mol dm^{-3}) against the selected metal ion (1.0×10^{-4} mol dm^{-3}), the Limit of Detection (LoD) and Limit of Quantification (LoQ) of compound **1** were similarly computed using equations of 3.3δ/K and 10δ/K, respectively [69]. The K was the slope of the fluorescence titration curve, and δ was calculated from the standard deviation of the means of nine data emission intensities of compound **1** at maxima. A fluorescence titration of the **1**+Cu^{2+} with EDTA was performed to determine the reversibility of compound **1** against Cu^{2+} [70-72]. Before and after the chelation with the Cu^{2+}, the emission quantum yield (ϕ_{em}) of compound **1** was determined using a relative value [51] compared to the standard of quinine sulphate in 0.5 M H_2SO_4 (ϕ_{em} = 0.546) [73].

Computational calculation

The computational calculations were performed using DFT and TD-DFT methodologies within the Gaussian 09 software. A theory level of Becke's three-parameter hybrid exchange function with the Lee-Yang-Parr gradient-corrected correlation functional (B3LYP) and a basis set of 6-311g+(d,p) was further utilized to complete the calculation [74,75]. A solvent of N, N-dimethylformamide (DMF)/H_2O was incorporated into the calculation based on the integral equation formalism of the polarizable continuum model (IEFPCM) to mimic the experimental environment [49,76]. The geometrical structures of the probe and its products at the S_0 and S_1 states were independently optimized to get the related parameters. The calculated infrared wavenumber and UV/Vis absorption spectra were compared to the measured ones to validate the calculation method further. The HOMO and LUMO molecular orbitals, as well as their energy band gap ($\Delta E_{HOMO\text{-}LUMO}$), were calculated at the same theoretical level. The frontier molecular orbital (FMO) theory [14,77,78] was used to study and analyze the energy data of the HOMO-LUMO states produced from the optimized molecular geometry of the enol-keto form of compounds **1** and **1**+Cu^{2+}. Thus, it is possible to assess the manifestation of the excited-state intramolecular proton transfer (ESIPT) mechanism. Generally, this type of intramolecular hydrogen bonding (IHB) must be verified at the ground state before proceeding with the ESIPT process. The IHB will be more stable when the bond length of the phenolic moiety's acidic proton donor (O-H) is longer, and the imine Schiff base's proton acceptor (H---N) is shorter. Furthermore, the achievement of the ESIPT is made possible by the reduced band-gap between the excited keto form (K*) and the excited enol form (E*), as well as the lower LUMO of K* compared to E* [49,53].

Results and discussion

Synthesis of compound 1

The compound **1** was successfully synthesized in a two-step reaction via precursor **2,** yielding an overall chemical yield of 26% (**Scheme 1**). A typical, straightforward Schiff base synthetic method [39,51,79] was also applied to compound **1**. Thus, no extensive purification was required, yielding a pure yellowish solid. Further elaborative spectroscopic elucidation was employed to confirm the structure of compound **1**. A specific Schiff base marker of a double imine bridge at the center of compound **1** was supported by the IR vibrations of C=N at 1,602, in addition to the stretching vibration of C-H sp^2 at 3,106, C=C aryl at 1,534, and C-O β-naphthol at 1,299 cm^{-1} (**Figure S1**). Apart from all IR signals, none of the wavenumbers were associated with the phenolic functional group. As reported elsewhere, a similar type of observation was attributed to an intramolecular hydrogen bonding effect [51].

To find out the type of protons constructed in the skeleton of compound **1**, a ^{1}H-NMR characterization was recorded in $CDCl_3$ (**Figure S2**), revealing the 6 proton signals appearance of the naphthalenic ring at 8.17 - 7.39 ppm of chemical shifts, 2 azomethine protons at 9.68 and 8.73 ppm, a downfield signal of -OH moiety

at 13.14 ppm, and two more protons of 4-bromothiophene at 7.24 and 7.41 ppm, respectively. Commonly, a free phenolic -OH is found at 9.95 ppm [80]. However, in an aprotic solvent like $CDCl_3$, the intramolecular hydrogen bonding of a phenolic -OH with an imine nitrogen was more pronounced in compound **1**. Thus, the phenolic -OH signal of compound **1** was further shifted to 13.14 ppm, as reported for other analogs elsewhere [80,81]. Consequently, the isomer geometry of the C_{11}=N_{13} was probably *E*, as verified elsewhere for a typical 2-hydroxy imine moiety [79]. However, as the -N-N- bond connects 2 imine moieties that are freely rotating, the other imine geometry was not well-established [79]. To complement the ^{1}H-NMR data, the ^{13}C-NMR spectra were subsequently obtained (**Figure S3**). Sixteen carbon signals were recorded, including four thiophene carbons at 108.18, 110.80, 134.33, and 139.53 ppm, two azomethine carbons at 153.38, and 161.33 ppm, respectively, and 10 aromatic carbons at 119.16, 120.11, 123.80, 127.41, 127.99, 128.17, 129.19, 132.75, 134.96, and 162.09 ppm. Overall, the NMR spectra did not reveal any other trace compounds that might have formed during synthesis and further interfered with the photophysical properties of the **1**-sensing.

Applying positive electrospray ionization to high-resolution mass spectrometry, the molecular weight was finally confirmed at *m/z* 358.9851, deviating by 0.8 ppm from the theoretical value (**Figure S4**). The measured *m/z* assigned a 12 of DBE, involving 2 naphthalene rings, one thiophene ring, and 9 C sp^2. Isotopic trace of bromide was revealed by a twin ionization mass peak at *m/z* of 358.9851 and 360.9817, with abundance ratio of 1:1. Thereby, the molecular formula of **1** was asserted as $[C_{16}H_{11}BrN_2OS\text{-}H]^+$.

Photophysical properties of compound 1

To investigate the photophysical properties of compound **1**, the absorption spectra of the compound were measured in a polar aprotic solvent of DMF at a total concentration of 1.0×10^{-5} mol dm^{-3}. A typical n to π* excitation band was assigned at λ_{max} 395 nm (19,300 ε/mol^{-1} dm^3 cm^{-1}) (**Figure 1**), plausibly attributed to the imine (Schiff base) and phenolic moieties. In addition, the presence of conjugated naphthalenic and azomethine resulted in a prominent π to π* transition at λ_{max} 338 nm (14,900 ε/mol^{-1} dm^3 cm^{-1}). A comparable spectra profile for compound **1** was also observed in other aprotic solvents, including DMSO, dioxane, dichloromethane, and chloroform (**Figure S5**).

In contrast, the maxima at 395 nm were shifted batochromically to 414 nm (6,800 ε/mol^{-1} dm^3 cm^{-1}) upon the addition of a more polar protic solvent of H_2O to DMF in a ratio of 9:1 (**Figure 1**). This bathochromic shift is attributed to enhanced stabilization of the ground state (S_0) via solvent-solute interactions. The preferential stabilization of compound **1** in its ground state (S_0) over the excited state (S_1) is likely due to more effective hydrogen bonding and solvation interactions in the presence of water compared to DMF alone [82]. However, since the hydrogen acceptor capability of DMF toward compound **1** was reduced with an increase in the water concentration, the molar absorptivity of the maxima at 414 nm was decreased almost three times lower than the original at 395 nm.

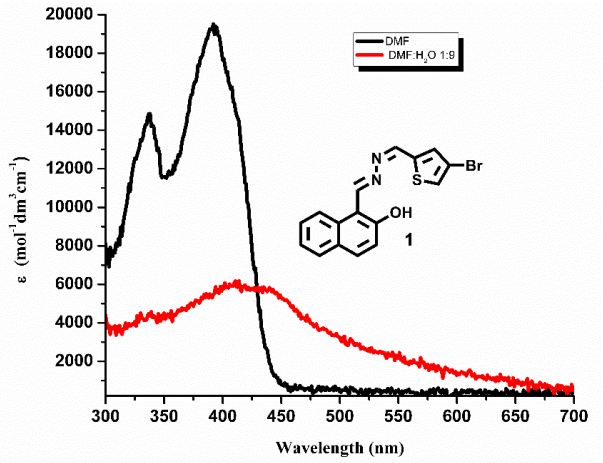

Figure 1 Absorptivity of compound **1** (1.0×10^{-5} mol dm^{-3}) in DMF:H_2O (1:9, *v/v*) (Red line), in DMF (Black line).

As the emission spectrum profile of the b-naphthol Schiff base, a typical fluorophore, is commonly exhibited upon a specific excitation wavelength, further analysis of the photophysical and sensing properties of compound **1** at 360 nm [69,70] is warranted. Analysis of a colloidal mixture **1** at a total concentration of 1.0×10^{-4} mol dm^{-3} at λ_{ex} of 360 nm revealed a quenching emission of λ_{em} 515 nm in DMF. The emission was even faded out at a clear solution **1** at a more diluted concentration (**Figure 2-Left**). In contrast, 14 times emission enhancement (ϕ_{em} = 0.252±0.030) and a 50 nm redshift emerged at the emission spectra of **1** in DMF:H_2O (1:9, *v*/*v*) compared to DMF (**Figure 2-Right**). It was observed that this phenomenon became negligible when probe **1** was used at lower concentrations. Most probably, the energy transfer of DMF toward the **1** in the excited state was attributed to the quenching process, as previously discovered elsewhere [83]. However, in some instances, a Schiff base-based sensor may exhibit aggregation-induced emission (AIE) at increased concentrations of water in organic solvent mixtures [72,73]. This confirmed the activation of emission due to aggregation.

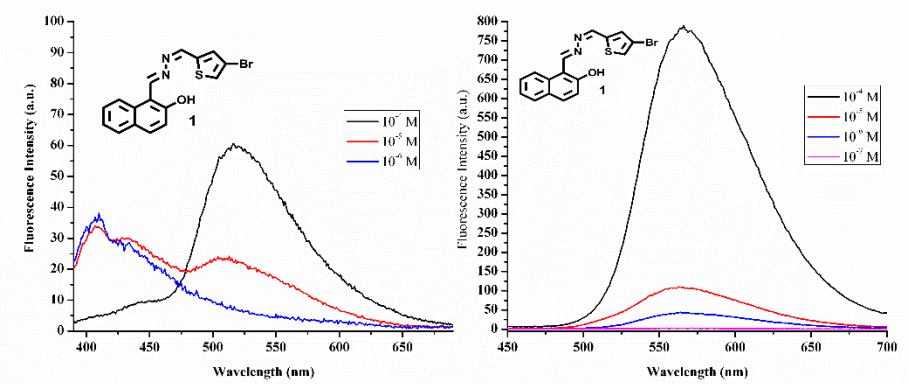

Figure 2 Fluorescence spectra of compound **1** at various concentrations: (Left) (1.0×10^{-4} - 1.0×10^{-6} mol dm^{-3}, λ_{ex} 360 nm) in DMF, (Right) (1.0×10^{-4} - 1.0×10^{-7} mol dm^{-3}, λ_{ex} 360 nm) in DMF:H_2O (1:9, *v*/*v*).

To confirm the AIE phenomenon, an analysis of the emission spectra of compound **1** under a binary solvent of DMF and increased water content (0% to 90%) with a total concentration of 1.0×10^{-4} mol dm^{-3} was performed (**Figure 3 (Left)**). A colloidal mixture of **1** was initially formed at a water content of 50% to 90%, followed by an enhanced emission. It was implied that a colloidal mixture was formed due to the aggregation of compound **1** at high concentration, which further induced enhanced emission. In addition, a bathochromic shift was distinctly observed when the water content increased from 40% to 50%, confirming a typical J aggregation [74].

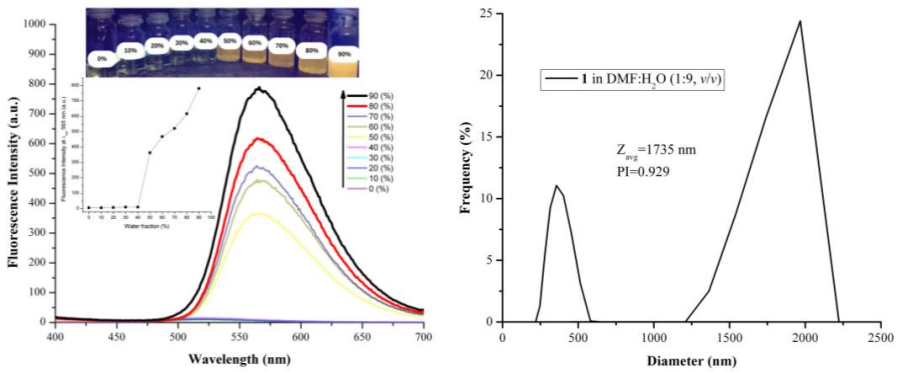

Figure 3 Emission spectra of compound **1** in a mixture of DMF and increased H_2O content (0-90%, *v*/*v*), (c_{total} = 1.0×10^{-4} mol dm^{-3}), λ_{ex} 360 nm. Inset: Fluorescence Intensity of water fraction at λ_{em} 565 nm (Left). DLS-Particle Size Distribution Analysis of compound **1** in 90% water fraction (Right).

Further dynamic light scattering (DLS) experiments verified the formation of larger aggregates of the probe in higher water fractions (**Figure 3 (Right)**). The results showed that the average particle size of compound **1** in 90% water/DMF was 1,735 nm, substantially different from the original clear solution of compound **1** in 100% DMF. The aggregates' polydispersity index (PI) values, larger than 0.7 [84], revealed a typical broad-size particle distribution of compound **1**, which was shaped**.** It was implied that the accumulation of particles associated with solvent molecules was increased upon an increase in water fraction. However, based on the first-order kinetic analysis of the emission change over time (**Figure S6**), the aggregation fell apart, with a $t_{1/2}$ of 29 minutes. The half-life may be prolonged under non-stirred conditions, thereby improving its potential for extensive applications.

Regardless of any solvation effect, the basic skeleton of the β-naphthol chromophore exhibited no emission because of a photoinduced electron transfer from the -OH moiety to the naphthalic fluorophore. In fact, a proton acceptor of -C=N adjacent to an -OH proton donor found at compound **1** potentially experienced a solid intramolecular hydrogen bonding [85]. Furthermore, the dominant solvatochromic effect of water (HBD constant of 1.17) [86] on compound **1** even strengthened an existing intramolecular hydrogen bonding, which commonly promotes intramolecular proton transfer at the excited state (ESIPT) [53,87,88]. Therefore, the photoinduced electron transfer was hindered, and the fluorescence of compound **1** was sparked. In particular, the ESIPT mechanism may preserve the planarity of compound **1** via an intramolecular rotational restriction and extend the conjugation system of compound **1** [56,89]. Finally, it may also induce the coupling aggregation-induced emission mechanism [51, 80-82], exhibit fluorescence properties similar to those of compound **1** at high concentrations, and have a physical appearance (**Figure 4**). This type of phenomenon is well known as AIE-coupled ESIPT, as reported in previous studies [46,90].

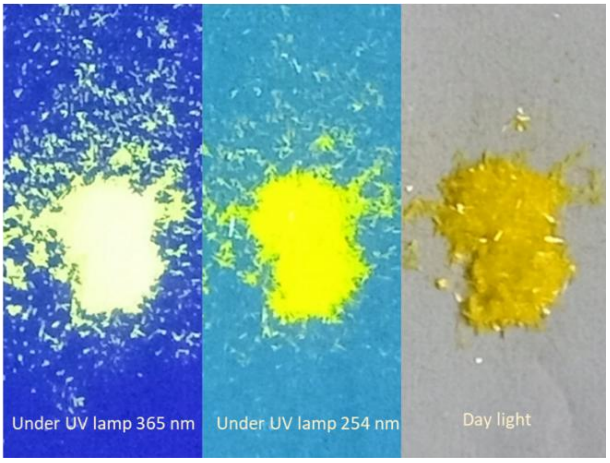

Figure 4 Fluorescence properties of compound **1** in the solid state over UV lamp at 365, 254 nm, and daylight.

Since the ESIPT process caused compound **1** to exhibit a significant Stokes shift ($\Delta\lambda$) of up to 173 nm in DMF and 151 nm in a 1:9 (*v*/*v*) DMF:H_2O mixture (**Figure S7**), which is beneficial for fluorescence imaging properties such as contrast [91]. Finally, based on the feasible solubility of compound **1** in a more aqueous system with excellent fluorescence properties, the combination of DMF:H_2O (1:9, *v*/*v*) system was further used for the probe's sensing assay.

Sensing nature of compound 1 against metal ions

The sensing assay of **1** in DMF:H_2O (1:9, *v*/*v*) against several representative cations including K^+, Li^+, Ag^+, Mg^{2+}, Ni^{2+}, Cu^{2+}, Zn^{2+}, Co^{2+}, Cd^{2+}, Hg^{2+}, Pb^{2+}, Fe^{2+}, Al^{3+}, and Cr^{3+} exhibited a typical chelating quenched fluorescence (CHQF). A diminishing bright yellow fluorescence of compound **1** was monitored upon mixing with the metal ions at 365 nm of UV light (**Figure 5-bottom**), and a transparent yellow color transition was observed under ambient light (**Figure 5-**

top). In particular, an intensive quenching of the fluorescence of compound **1** was demonstrated against Cu^{2+} at a 1:1 ratio. Spectrofluorimetric corroboration was further pursued for the prospective chelating properties of compound **1**, using a specific cation in the qualitative assay. Upon a 1:1 mol ratio, all the metal ions quenched the compound **1** to a certain degree. Most of the transition and post-transition metal ions, such as Ag^{+}, Cd^{2+}, Cr^{3+}, Hg^{2+}, Ni^{2+}, Al^{3+}, and Pb^{2+}, quenched the probe **1** emission by less than 15%, compared to the parent relative intensity, while ions of Li^{+}, Zn^{2+}, Fe^{2+}, and Co^{2+} were less than 50%. In fact, a distinctive emission quenching of compound **1** at 565 nm was demonstrated against Cu^{2+} (**Figure 6)**.

Figure 5 Qualitative test of compound **1** against representative cations in DMF:H_2O (1:9, *v/v*) (c_{total} = 1.0 x 10^{-4} mol dm^{-3}) over ambient light (top) and 365 nm UV light (bottom).

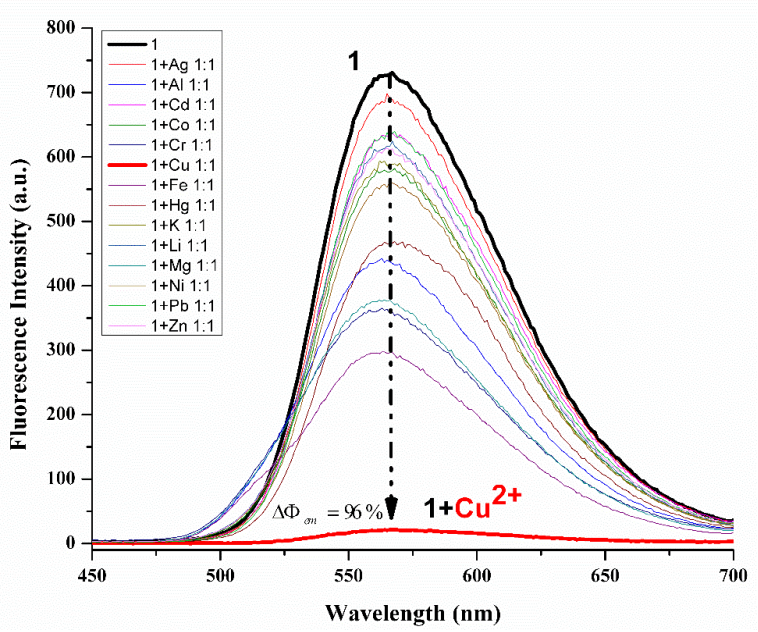

Figure 6 Fluorescence spectra of compound **1** against various metal ions in DMF:H_2O (1:9, *v/v*) (c_{total} = 1.0×10^{-4} mol dm^{-3}) at λ_{ex} 360 nm and λ_{em} 565 nm.

A quantum yield of emission was subsequently determined, verifying the quenching process of compound **1** against Cu^{2+} up to 96% ((ϕ_{em} of **1**=0.252±0.030; **1**+Cu^{2+}=0.012±0.004) (**Figure S8**). Since the intensive emission of compound **1** is most likely caused by the PET inhibition of the naphthalenic fluorophore due to an ESIPT process, the strong coordination of compound **1** with the Cu^{2+} metal ion might interrupt the ESIPT and allow the PET to occur. Thereby, the emission of compound **1** was tremendously quenched by the Cu^{2+} ion. A similar mechanism has been reported elsewhere for a typical Schiff base chemosensor [89]. Since the Cu^{2+} decreased the emission intensity of compound **1** distinctly, it could be

employed for naked-eye detection. Thereby, compound **1** was a typical "on-off" sensor.

Regarding selectivity, compound **1** was a reasonably distinguished Cu^{2+} ion to a certain degree from other representative ions (**Figure 7**). The chart bar showed that the fluorescence strength of **1**+Cu^{2+} was affected by other contaminated metal ions, with a relative fluorescence intensity (FI) increase of up to 15%, especially by Ag^{+}, Cd^{2+}, Fe^{2+}, Ni^{2+}, Pb^{2+}, K^{+}, Li^{+}, Mg^{2+}, and Zn^{2+}. Fewer interferences (< 5%) were demonstrated by Cr^{3+}, Hg^{2+}, and Al^{3+}. Plausibly, probe **1** can be applied as a Cu^{2+} sensor for samples free of $Co^{2+,}$ which disrupts the fluorescence intensity (FI) of **1**+Cu^{2+} by up to 20%. A Job's plot analysis was then followed to determine the binding ratio between **1** and Cu^{2+}. Upon a constant total concentration of 1.0×10^{-4} mol dm^{-3}, an emission spectrum of a mixture of **1**+Cu^{2+} at a ratio of 0.1 to 0.9 was obtained, revealing a securely established complex at a molar ratio of 1:1 (**Figure 8**). An HRMS-ToF analysis further highlighted the 1:1 complex of **1**+Cu^{2+} measured in ES^{-} with its isotopic traces of Br^{79} and Br^{81} (*m/z*: $[C_{16}H_{10}Br^{79}CuN_2OS]^{-}$: 419.7022, $[C_{16}H_{10}Br^{81}CuN_2OS]^{-}$: 421.0466) (**Figure S9**).

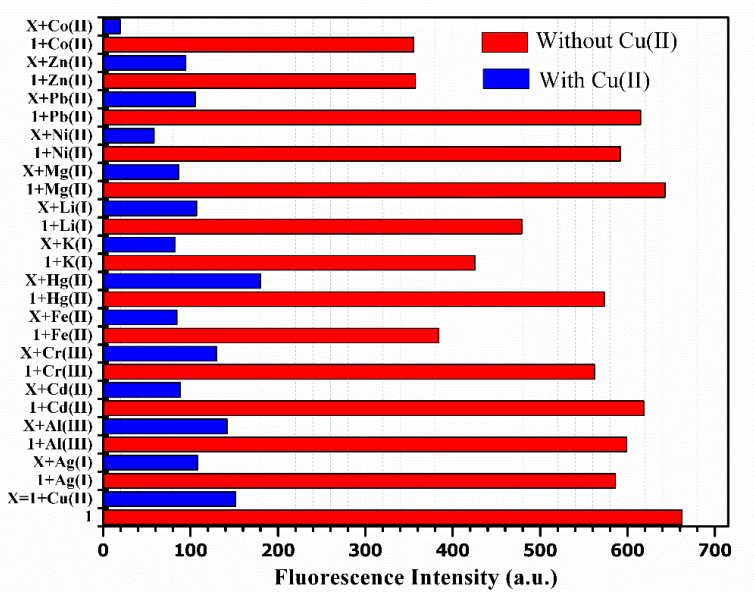

Figure 7 Changes of fluorescence intensity of **1**+Cu^{2+} (1:1, *v/v*) in the presence of 1 eq of other competitive cations [c_{total} 1.0×10^{-4} mol dm^{-3} in DMF:H_2O (1:9, *v/v*)] (λ_{ex} 360 nm, λ_{em} 565 nm).

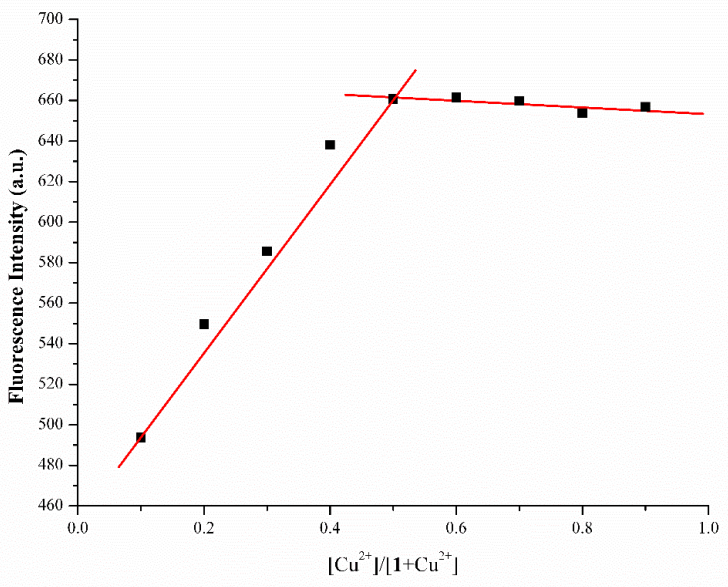

Figure 8 Job's Plot of **1** with Cu^{2+} ion in DMF:H_2O (1:9, *v/v*) (c_{total} 1.0 x 10^{-4} mol dm^{-3} (λ_{ex} 360 nm, λ_{em} 565 nm).

A fluorescence titration of the ion over compound **1** was performed to determine the detection limit against the Cu^{2+} ion in aqueous DMF. According to the linear regression of the plotted data (slope/K: 1.7119×10^{8}; STDV/δ: 31.4389) assisted by the 3.3δ/K and 10δ/K equations [69], the LoD and LoQ of compound **1** were discovered at 0.606 µM and 1.836 µM, respectively (**Figure 9, Figure S10**).

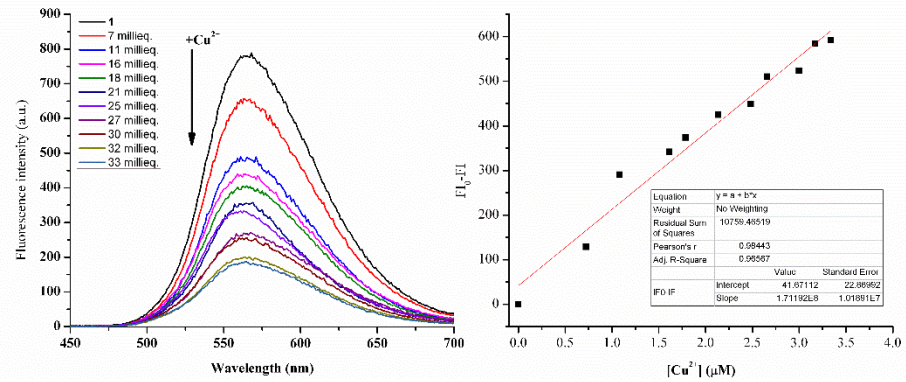

Figure 9 Titration curve of fluorescence of compound **1** (1.0×10^{-4} mol dm^{-3}) in DMF:H_2O (1:9, *v/v*) vs Cu^{2+} ions at ambient temperature (λ_{ex} 360 nm) (Left). Linear regression of fluorescence degradation at 565 nm as a function of Cu^{2+} concentration (Right).

A high binding constant of the complex in DMF:H_2O (1:9, *v/v*) was further calculated (3.95×10^{6} M^{-1}) from the titration experiment of UV/Vis absorbance (**Figure 10**) and the Benesi-Hildebrand equation [67,68]. The isosbestic point of the titration spectra was barely visible. It was implied that a transformation occurred during the titration, possibly due to the aggregation changes of the involved species [92-94].

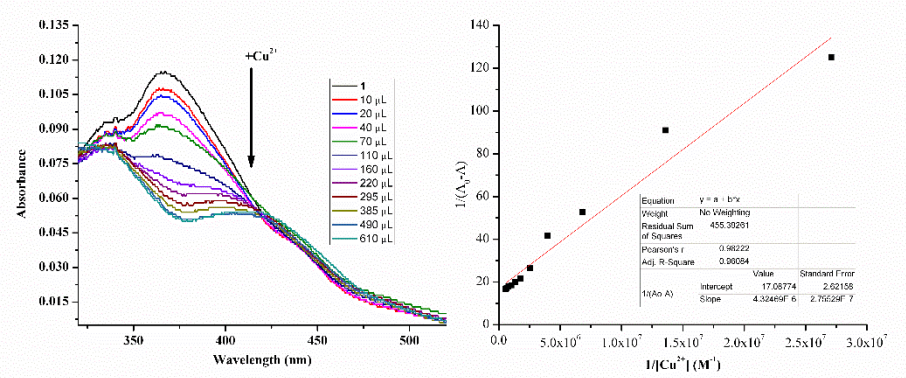

Figure 10 Titration curve of UV absorbances of compound **1** (5×10^{-5} mol dm^{-3}) with Cu^{2+} (1×10^{-5} mol dm^{-3}) (Left), Benesi-Hildebrand plotting data of compound **1** with Cu^{2+} ion in DMF:H_2O (1:9, *v/v*) at λ_{max} 367 nm (Right).

The reversibility of sensor compound **1** against Cu^{2+} was then investigated using a complexing agent, such as EDTA [70,71] (**Figure 11**). The fluorescence recovery percentage (FRP) of compound **1** quenched by Cu^{2+} ions showed a decreasing tendency after three cycles. Hence, the chemosensor of compound **1** exhibited partial reversibility against Cu^{2+} ions to a certain degree.

.

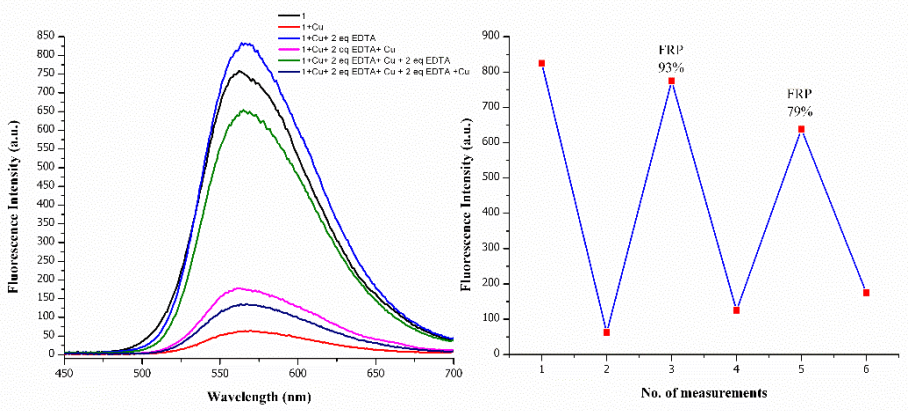

Figure 11 Reversibility experiment of compound **1** (1.0×10^{-4} mol dm^{-3}) in DMF:H_2O (1:9, *v/v*) against Cu^{2+} ions and EDTA at ambient temperature (λ_{ex} 360 nm) (Left). Fluorescence changes at 565 nm and their fluorescence recovery percentage (FRP) (Right).

The potential application of compound **1** as a paper-based strip probe of Cu^{2+} indicator was further demonstrated at a preliminary step. After immersing a Whatman filter paper into probe compound **1** (1.0×10^{-3} mol dm^{-3}) in DMF:water (1:9, *v/v*) solution 5 times, compound **1** was absorbed. Afterward, the dry paper immobilized by compound **1** was tested against a Cu^{2+} ion solution at a similar concentration in deionized water and photographed digitally under a UV lamp at 365 nm [95,96]. The observed results showed a bright fluorescence emission of compound **1** before it was dipped into the Cu^{2+} ion solution (**Figure 12-Before**). Once paper-test of compound **1** was immersed in the Cu^{2+} solution, the bright fluorescence of paper-test compound **1** decreased (**Figure 12-After**). Therefore, compound **1** will likely be used for the visual and qualitative detection probe of Cu^{2+} metal ions, offering good performance and simplicity without requiring complex equipment. A preliminary stability test of the paper-based sensor conducted over several days at ambient conditions revealed a consistent fluorescence response. However, further studies under controlled humidity and temperature conditions are still necessary to evaluate its long-term performance comprehensively.

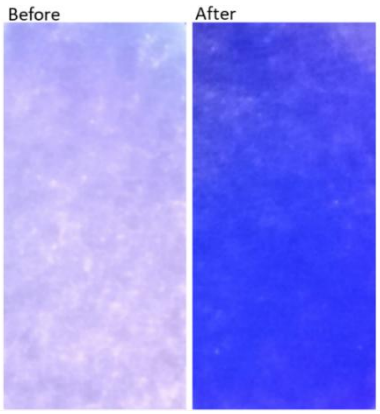

Figure 12 A Whatman filter paper immobilized by compound **1** (1.0×10^{-3} mol dm^{-3}) in DMF:water (1:9, *v/v*) before and after being tested against Cu^{2+} ions solution (1.0×10^{-3} mol dm^{-3}) in demineralized water. The visualization was under a UV lamp at 365 nm.

Since the response of probe **1** against Cu^{2+} was based on the difference in blue fluorescence intensity, a more rigorous investigation of the paper-based strips is necessary. For instance, a calibrated paper-based strip fluorescence quenching index of **1**+Cu^{2+} can be prepared in the presence of individual ion contaminants. Synchronous fluorescence spectroscopy should be a suitable method for the FI calibration of the paper test

[97,98]. Employing a digital camera to photograph the prepared strips and determine their RGB values under a 365 nm UV lamp may simplify its application prospects for a real-time qualitative test. The previous finding [27,96,99,100] demonstrated that the fluorescent response of a paper-based sensor can be captured using a standard smartphone camera under 365 nm UV illumination. The RGB values are then extracted and analyzed to convert the visual fluorescence change into a semi-quantitative signal, eliminating the need for complex instrumentation.

According to the aforementioned experimental data, the interaction of compound **1** with the Cu^{2+} ion most probably occurred through inhibition of the IHB with the ion, as proposed in **Figure 13**. Afterward, an inhibition of ESIPT, which commonly occurred in particular Schiff base derivatives, might be the most rational sensing mechanism [51,71,89]. Therefore, further computational analysis of probe **1** was performed.

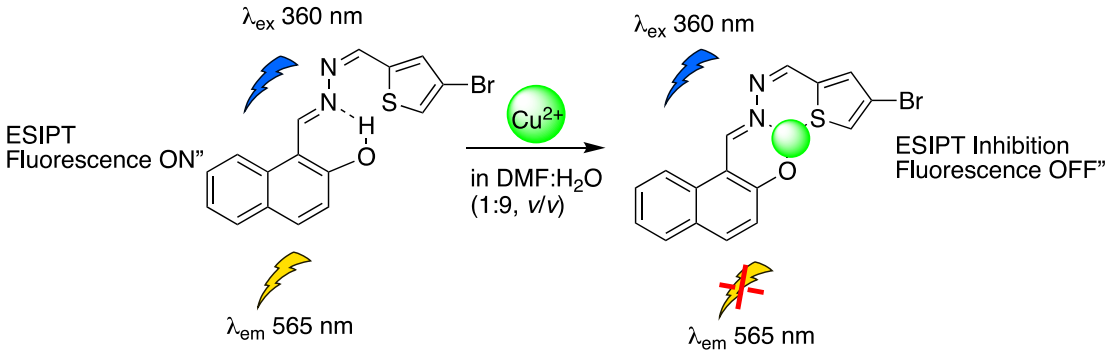

Figure 13 A proposed interaction mechanism of **1** with Cu^{2+} ion.

In Silico study of the ESIPT of probe 1 and its interaction with Cu^{2+} ion

Upon a geometry optimization of compound **1,** at the B3LYP level of theory and 6-311g+(d,p) basis set, positive vibrational frequencies (IR) of compound **1** were recorded (**Figure S11**). Thus, a minimum state of compound **1**, which indicated a stable form, was achieved (**Figure 14**). Some representative moieties, namely as stretching of -OH, C=N, and aromatic C=C at 3,250, 1,642, and 1,578 cm^{-1}, respectively, emerged. The calculated values of compound **1** deviated by 31 - 107 cm^{-1}, which is within acceptable computational margins. In addition, further calculation verification was achieved by comparison of the computed UV/Vis spectra profile of the **1**-enol and **1**-keto with the measured ones (**Figure S12**). Overall, the calculation method demonstrated accuracy that closely approximated the experimental results, providing reasonable verification of its validity.

To confirm the ESIPT process of compound **1,** which leads to the isomerization of enol-keto, we examined the optimized structures of **1**-enol and **1**-keto in further detail. Since intramolecular hydrogen bonding (IHB) involves the bonds at the O_{19}, H_{20}, and N_{21} atoms (**Figure 14**), changes in bond length and angle upon excitation should be observed [101,102]. It was implied that bond elongation of the O_{19}-H_{20} of **1**-E (0.031 Å) was distinctively revealed upon excitation to S_1. On the other hand, a bond shortening was also observed at the H_{20}-N_{21} of **1**-E (0.116 Å). In addition, a widening angle (20°) of O_{19}-H_{20}---N_{21} close to 180° was also assigned, along with the bond length change. For comparison, analogous changes were also demonstrated by the **1**-K upon excitation (**Figure 14, Table S1**). Consequently, an IHB of phenol O_{19}-H_{20} toward imine N_{21} was strongly enhanced upon excitation. As the **1**-enol was more stable than the **1**-keto by 3.29 kcal/mol in S_0 and 0.658 kcal/mol in S_1 (**Table S2**), the **1**-enol form might have dominantly occurred at the S_1 state.

Further analysis of the frontier molecular orbital (FMO) toward **1** enol/E and keto/K (**Figure 15**) highlighted the presence of an enol-keto tautomerism in compound **1**. The study revealed that **1**-keto (3.21 eV) had a lower energy band-gap than **1**-enol (3.38 eV). A redistribution of **1**-E and **1**-K electronic density upon excitation was also observed. The electron density of the N_{21} and O_{19} at LUMO of **1**-E* and **1**-K*, respectively, was increased. These changes enhanced the proton

acceptor capability of the related atoms at the S_1 state. Since the LUMO energy of **1**-K* was also, relatively lower than the **1**-E*, the ESIPT was finally favorable to occur, as it was accordingly found in the other typical Schiff base [49,51,53,103]. On the other hand, when the Cu^{2+} ion was chelated by compound **1**, the IHB was replaced by the ions, and the keto-enol tautomerization was restricted (**Figure S13**). Finally, the original inhibited photoinduced electron transfer was released, and the fluorescence of compound **1** was quenched irreversibly. Overall, according to the computational calculation of **1**-enol, **1**-keto, and their chelated complex, the ESIPT phenomena and the interaction mechanism were further verified theoretically, and the result aligned with similar findings reported elsewhere [14,53,58,89]. Employing advanced techniques like transient absorption spectroscopy would offer additional confirmation of the ESIPT mechanism and allow for precise determination of its kinetic parameters [104,105].

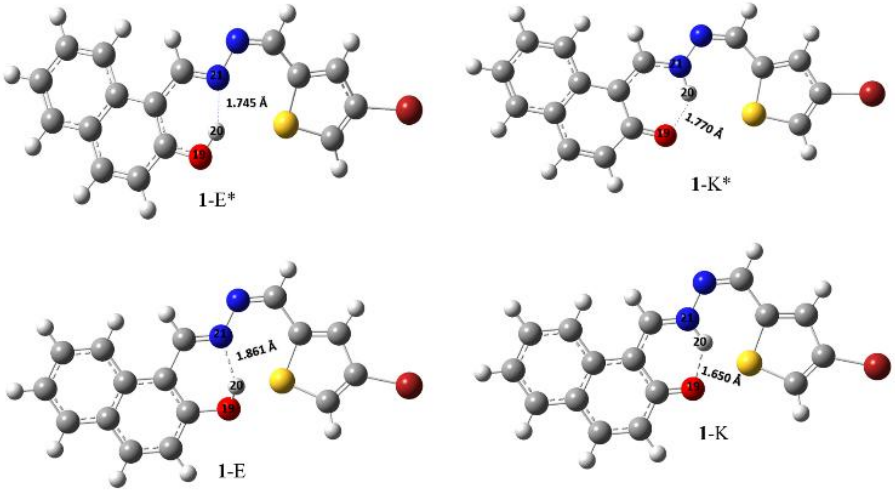

Figure 14 Optimized geometry structures of **1**-E and **1**-K at the states of S_0 and S_1.

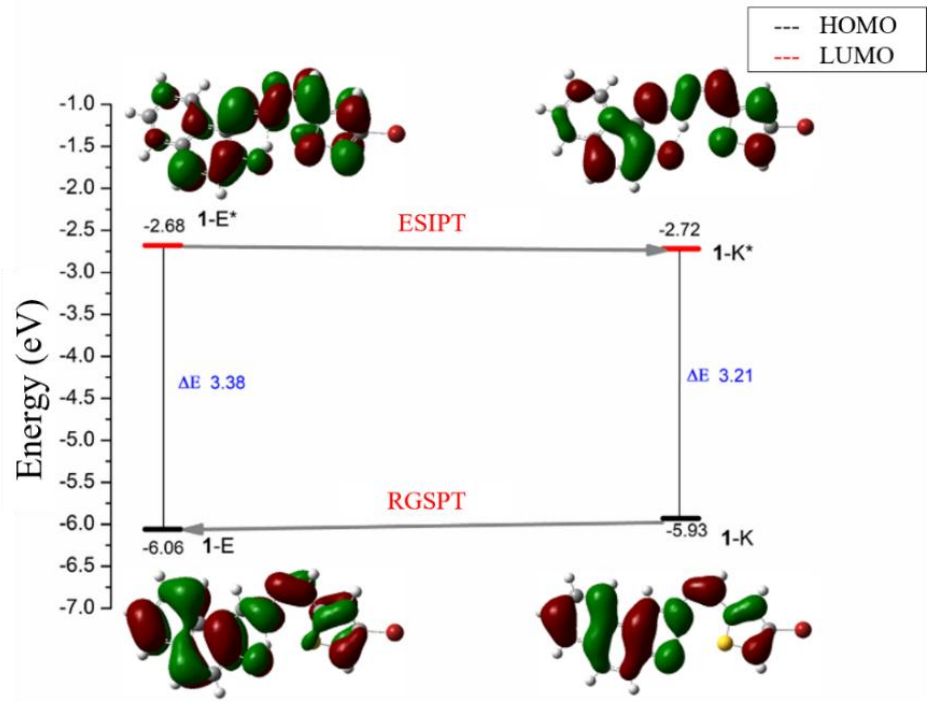

Figure 15 Calculated frontier molecular orbital of enol-keto of **1** and its energy band-gap.

Conclusions

A Novel AIE-ESIPT-based chemosensor of 1-((((4-bromothiophen-2-yl)methylene)hydrazineylidene)methyl) naphthalen-2-ol (**1**) was successfully synthesized and characterized based on the spectroscopic analysis. Compound **1** demonstrated a limited selectivity on-off sensor against Cu^{2+} ion in DMF:H_2O (1:9, *v*/*v*) at 1:1 molar ratio binding mode, with the LoD and LoQ being 0.606 μM and 1.836 μM. Upon experimental and computational study, sensor **1** was confirmed to undergo an ESIPT process, followed by inhibition against Cu^{2+} ions. Therefore, compound **1** might be further applied to detect Cu^{2+} ions in an aqueous system under particular conditions.

Acknowledgements

The author would like to thank Universitas Padjadjaran for the support of the RKDU and ALG Grant (1984/UN6.3.1/PT.00/2024). The authors also extend their gratitude to the Laboratory of Integrated Chemistry at the Institute of Technology Bandung for the NMR measurements and to the Central Laboratory of Universitas Padjadjaran for the fluorimetry experiments.

Declaration of Generative AI in Scientific Writing

The authors acknowledge the use of the generative AI tool “Grammarly” in the preparation of this manuscript, specifically for language editing and grammar correction. No content generation or data interpretation was performed by AI. The authors take full responsibility for the content and conclusions of this work.

CRediT Author Statement

Dessy Eka Putri Romadhon: Data curation; Writing - Original draft preparation; Visualization; Investigation; Formal Analysis. **Rizka Permata**: Data curation; Writing - Original draft preparation; Visualization; Investigation. **Juliandri**: Conceptualization; Methodology; Software; Validation; Supervision. **Dadan Sumiarsa**: Conceptualization; Methodology; Resources. **Rani Maharani**: Conceptualization; Methodology; Resources. **Ace Tatang Hidayat**: Conceptualization; Methodology; Project administration and Funding acquisition. **Jamaludin Al-Anshori**: Conceptualization; Methodology; Supervision; Writing - Reviewing and Editing; Project administration and Funding acquisition.

References

[1] NA Al-Rawashdeh. *Current achievement and future potential of fluorescence spectroscopy*. *In*: J Uddin (Ed.). Macro to nano spectroscopy. InTech, Rijeka, Croatia, 2012, pp. 209-250.

[2] JMR Antoine, LAH Fung, CN Grant, HT Dennis and GC Lalor. Dietary intake of minerals and trace elements in rice on the Jamaican market. *Journal of Food Composition and Analysis* 2012; **26(1-2)**, 111-121.

[3] YW Choi, GJ Park, YJ Na, HY Jo, SA Lee, GR You and C Kim. A single schiff base molecule for recognizing multiple metal ions: A fluorescence sensor for Zn(II) and Al(III) and colorimetric sensor for Fe(II) and Fe(III). *Sensors & Actuators: B. Chemical* 2014; **194**, 343-352.

[4] Y Jeong and J Yoon. Recent progress on fluorescent chemosensors for metal ions. *Inorganica Chimica Acta* 2012; **381**, 2-14.

[5] X Chen, T Pradhan, F Wang, JS Kim and J Yoon. Fluorescent chemosensors based on spiroring-opening of xanthenes and related derivatives. *Chemical Reviews* 2012; **112(3)**, 1910-1956.

[6] MA Barakat. New trends in removing heavy metals from industrial wastewater. *Arabian Journal of Chemistry* 2011; **4(4)**, 361-377.

[7] D Wu, A Sedgwick, T Gunnlaugsson, EU Akkaya, J Yoon and TD James. Fluorescent chemosensors: The past, present and future. *Chemical Society Reviews* 2017; **46(23)**, 7105-7123.

[8] S Mitra, A Jyoti, A Montakim, T Bin, F Nainu, A Khusro, AM Idris, M Uddin, H Osman, FA Alhumaydhi and J Simal-gandara. Impact of heavy metals on the environment and human health: Novel therapeutic insights to counter the toxicity. *Journal of King Saud University - Science* 2022; **34(3)**, 101865.

[9] S Sakunkaewkasem, A Petdum, W Panchan, J Sirirak, A Charoenpanich, T Sooksimuang and N Wanichacheva. Dual-Analyte fluorescent sensor based on [5]Helicene derivative with super large

stokes shift for the selective determinations of Cu^{2+} or Zn^{2+} in buffer solutions and its application in a living cell. *ACS Sensors* 2018; **3(5)**, 1016-1023.

[10] S Wang, Z Sheng, Z Yang, D Hu, X Long, G Feng, Y Liu, Z Yuan, J Zhang, H Zheng and X Zhang. Activatable small-molecule photoacoustic probes that cross the Blood-Brain barrier for visualization of Copper(II) in mice with alzheimer's disease. *Angewandte Chemie - International Edition* 2019; **58(36)**, 12415-12419.

[11] J Sackey, M Akbari, N Tandjigora, KJ Cloete, AKH Bashir, R Morad and M Maaza. Science Industrial textile removal using date pit assisted CuO-MgO nanocomposite: Molecular dynamics and biosynthesis analysis. *Journal of King Saud University - Science* 2022; **34(3)**, 101840.

[12] PB Tchounwou, CG Yedjou, AK Patlolla and DJ Sutton. Heavy metal toxicity and the environment. *Molecular, Clinical and Environmental Toxicology* 2012; **101** 133-164.

[13] GK Kinuthia, V Ngure, D Beti, R Lugalia, A Wangila and L Kamau. Levels of heavy metals in wastewater and soil samples from open drainage channels in Nairobi, Kenya: Community health implication. *Scientific Reports* 2020; **10**, 8434.

[14] I Abdulazeez, C Basheer and AA Al-Saadi. A selective detection approach for Copper(II) ions using a hydrazone-based colorimetric sensor: Spectroscopic and DFT study. *RSC Advances* 2018; **8(70)**, 39983-39991.

[15] Y Lu, X Liang, C Niyungeko, J Zhou, J Xu and G Tian. A review of the identification and detection of heavy metal ions in the environment by voltammetry. *Talanta* 2018; **178** 324-338.

[16] M Shaban, AGA Hady and M Serry. A new sensor for heavy metals detection in aqueous media. *IEEE Sensors Journal* 2014; **14(2)**, 436-441.

[17] ZY Li, HK Su, K Zhou, BZ Yang, T Xiao, XQ Sun, J Jiang and L Wang. Oxo-spirocyclic structure bridged ditopic Schiff base: A turn-on fluorescent probe for selective recognition of Zn(II) and its application in biosensing. *Dyes and Pigments* 2018; **149**, 921-926.

[18] S Kim, H Lee, H So, H Lee, KT Kim and C Kim. A benzyl carbazate-based fluorescent chemosensor for detecting Zn^{2+}: Application to zebrafish. *Spectrochimica Acta - Part A: Molecular and Biomolecular Spectroscopy* 2020; **228**, 117787.

[19] F Liu, C Fan, Y Tu and S Pu. A new fluorescent and colorimetric chemosensor for Al^{3+} and F^{-}/CN^{-} based on a julolidine unit and its bioimaging in living cells. *RSC Advances* 2018; **8(54)**, 31113-31120.

[20] S Velmathi, V Reena, S Suganya and S Anandan. Pyrrole based schiff bases as colorimetric and fluorescent chemosensors for fluoride and hydroxide anions. *Journal of Fluorescence* 2012; **22(1)**, 155-162.

[21] B Naskar, R Modak, Y Sikdar, DK Maiti, A Bauza, A Frontera, A Katarkar, K Chaudhuri and S Goswami. Fluorescent sensing of Al^{3+} by benzophenone based Schiff base chemosensor and live cell imaging applications: Impact of keto-enol tautomerism. *Sensors and Actuators, B: Chemical* 2017; **239**, 1194-1204.

[22] H Han and D Pan. Voltammetric methods for speciation analysis of trace metals in natural waters. *Trends in Environmental Analytical Chemistry* 2021; **29**, 00119.

[23] Y Guo, H Zhao, Y Han, X Liu, S Guan, Q Zhang and X Bian. Simultaneous spectrophotometric determination of trace copper, nickel, and cobalt ions in water samples using solid phase extraction coupled with partial least squares approaches. *Spectrochimica Acta Part A: Molecular and Biomolecular Spectroscopy* 2017; **173**, 532-536.

[24] B Fernandez, L Lobo and R Pereiro. *Atomic absorpton spectrometry | fundamentals, instrumentation and capabilities*. 3rd ed. Elsevier Inc, New York, 2019, p. 137-143.

[25] SLC Ferreira, MA Bezerra, AS Santos, WNL dos Santos, CG Novaes, OMC de Oliveira, ML Oliveira and RL Garcia. Atomic absorption spectrometry - A multi element technique. *TrAC - Trends in Analytical Chemistry* 2018; **100**, 1-6.

[26] D Plausinaitis, B Knasiene, CA Vicent, P Aleksandr and N Evaldas. Simultaneous detection of Mn, Co, Ni, and Cu using ion chromatography coupled with ICP-MS with a special focus on the determination of ^{59}Ni in corrosion deposits. *Journal of Radioanalytical and Nuclear Chemistry* 2018; **316(1)**, 257-265.

[27] E Munoz and S Palmero. Determination of heavy metals in milk by potentiometric stripping analysis using a home-made flow cell. *Food Control* 2004; **15(8)**, 635-641.

[28] J Zhang, L Xu and WY Wong. Energy materials based on metal Schiff base complexes. *Coordination Chemistry Reviews* 2018; **355**, 180-198.

[29] M Lin, MS Cho, WS Choe and Y Lee. Electrochemical analysis of copper ion using a Gly–Gly–His tripeptide modified poly(3-thiopheneacetic acid) biosensor. *Biosensors and Bioelectronics* 2009; **25(1)**, 28-33.

[30] YZ Peng, YM Huang, DX Yuan, Y Li and ZB Gong. Rapid analysis of heavy metals in coastal seawater using preconcentration with precipitation/co-precipitation on membrane and detection with X-ray fluorescence. *Chinese Journal of Analytical Chemistry* 2012; **40(6)**, 877-882.

[31] LA Hutton, GD O'Neil, TL Read, ZJ Ayres, ME Newton and JV Macpherson. Electrochemical X-ray fluorescence spectroscopy for trace heavy metal analysis: Enhancing X-ray fluorescence detection capabilities by four orders of magnitude. *Analytical Chemistry* 2014; **86(9)**, 4566-4572.

[32] S Griesel, U Reus and A Prange. Electro-deposition as a sample preparation technique for total-reflection x-ray fluorescence analysis. *Spectrochimica Acta Part B: Atomic Spectroscopy* 2001; **56(11)**, 2107-2115.

[33] Q Fan and Y Gohshi. Enhancement of total reflection X-Ray fluorescence spectroscopy with electrochemical deposition. *Applied Spectroscopy* 1993; **47(11)**, 1742-1746.

[34] B Zawisza and R Sitko. Electrochemically assisted sorption on oxidized multiwalled carbon nanotubes for preconcentration of Cr, Mn, Co, Ni, Cu and Zn from water samples. *Analyst* 2013; **138(8)**, 2470-2476.

[35] F Zhao, Z Chen, F Zhang, R Li and J Zhou. Ultra-sensitive detection of heavy metal ions in tap water by laser-induced breakdown spectroscopy with the assistance of electrical-deposition. *Analytical Methods* 2010; **2(4)**, 408-414.

[36] Z Chen, H Li, F Zhao and R Li. Ultra-sensitive trace metal analysis of water by laser-induced breakdown spectroscopy after electrical-deposition of the analytes on an aluminium surface. *Journal of Analytical Atomic Spectrometry* 2008; **23(6)**, 871-875.

[37] C Guo, J Wang, J Cheng and Z Dai. Determination of trace copper ions with ultrahigh sensitivity and selectivity utilizing CdTe quantum dots coupled with enzyme inhibition. *Biosensors and Bioelectronics* 2012; **36(1)**, 69-74.

[38] PG Mahajan, NC Dige, BD Vanjare, E Kamaraj, SY Seo and KH Lee. Nano molar level chromogenic and fluorogenic sensing of heavy metal ions using multi-responsive novel Schiff base as a dual mode chemosensor. *Journal of Photochemistry and Photobiology A: Chemistry* 2019; **385**, 112089.

[39] A Kundu, PS Hariharan, K Prabakaran and SP Anthony. Synthesis of new colori/fluorimetric chemosensor for selective sensing of biologically important Fe^{3+}, Cu^{2+} and Zn^{2+} metal ions. *Spectrochimica Acta Part A: Molecular and Biomolecular Spectroscopy* 2015; **151**, 426-431.

[40] YL Liu, L Yang, P Li, SJ Li, L Li, XX Pang, F Ye and Y Fu. A novel colorimetric and "turn-off" fluorescent probe based on catalyzed hydrolysis reaction for detection of Cu^{2+} in real water and in living cells. *Spectrochimica Acta Part A: Molecular and Biomolecular Spectroscopy* 2020; **227**, 117540.

[41] MAFA Manan and MF Mohammat. Synthesis, structural studies and antimicrobial evaluation of Nickel(II) bis-complex of schiff base of S-Benzyldithiocarbazate. *Trends in Sciences* 2022; **19(23)**, 1500.

[42] J Wu, W Liu, J Ge, H Zhang and P Wang. New sensing mechanisms for design of fluorescent chemosensors emerging in recent years. *Chemical Society Reviews* 2011; **40(7)**, 3483-3495.

[43] K Mohammadiannejad, R Ranjbar-karimi and F Haghighat. Synthesis of azine- and hydrazone-based triarylmethanes. *Polycyclic Aromatic Compounds* 2019; **41(3)**, 1-12.

[44] MAFA Manan and DB Cordes. Cadmium(II) schiff base complex containing 5-Fluoroisatin moiety: Synthesis, Characterization, Antibacterial Activity and Structural Studies. *Trends in Sciences* 2022; **19(18)**, 5796.

[45] A Gupta, N Kumar, A review of mechanisms for fluorescent "turn-on" probes to detect Al^{3+} ions. *RSC Advances* 2016; **6(108)**, 106413-106434.

[46] R Kaur, R Kour, SS Marok and S Kaur. AIE+ESIPT active hydroxybenzothiazole for intracellular detection of Cu^{2+}: anticancer and anticounterfeiting applications. *Molecules* 2022; **27(8)**, 7678.

[47] X Wang, L Xu, H Gao and J Song. Construction of dehydroabietic acid triarylamine-based "ESIPT + AIE" type molecule for "On-Off" sensing of Cu^{2+} and anti-counterfeiting. *Journal of Photochemistry and Photobiology A: Chemistry* 2025; **469**, 116565.

[48] W Guo, Y Zhang, Y Wang, Z Hu, P Xu, J Cai, P Yu, S Chen, L Zhang, B Wei, J Zhang, S Li, H Wang and L Chen. A water-soluble fluorescent probe derived from fish collagen peptides for multi-targeted detection of Cu^{2+} and Zn^{2+} ions via AIE and ESIPT mechanisms. *Microchemical Journal* 2025; **215**, 114313.

[49] S Su and H Fang. Theoretical investigation on the ESIPT mechanism and fluorescent sensing mechanism of 2-(2′-hydroxyphenyl) thiazole-4-carboxaldeyde in methanol. *Spectrochimica Acta - Part A: Molecular and Biomolecular Spectroscopy* 2020; **233**, 118214.

[50] H Ibraheem, G El-Hiti, E Yousif, D Ahmed, B Kariuki, S Ismael and M Bufaroosha. Enhancing photostability of chemically modified Poly(Vinyl Chloride) through the incorporation of organotin moieties on the polymeric chains. *Trends in Sciences* 2025; **22(4)**, 9413.

[51] J Al-Anshori, D Ismalah, AF Abror, A Zainuddin, IW Hidayat, M Yusuf, R Maharani and AT Hidayat. A new highly selective "off-on" typical chemosensor of Al^{3+}, 1-((Z)-((E)-(3,5-dichloro-2-hydroxybenzylidene)hydrazono)methyl) naphthalene-2-ol, an experimental and *in silico* study. *RSC Advances* 2022; **12(5)**, 2972-2979.

[52] J Jayabharathi, V Thanikachalam, M Vennila and K Jayamoorthy. Potential fluorescent chemosensor based on L-tryptophan derivative: DFT based ESIPT process. *Spectrochimica Acta - Part A: Molecular and Biomolecular Spectroscopy* 2012; **95**, 446-451.

[53] AA Jamaludin, M Aenal, HI Wiani, Z Achmad and HA Tatang. Synthesis and ESIPT phenomena of a new β-Naphthol derivative, an experimental and *in silico* study. *Research Journal of Chemistry and Environment* 2022; **26(8)**, 88-97.

[54] MJ Frisch, GW Trucks, HB Schlegel, GE Scuseria, MA Robb, JR Cheeseman, G Scalmani, V Barone, GA Petersson, H Nakatsuji, X Li, M Caricato, AV Marenich, J Bloino, BG Janesko, R Gomperts, B Mennucci, HP Hratchian, JV Ortiz, AF Izmaylov, …, DJ Fox. *Gaussian 16. Revision C.01*. Expanding the limits of computational chemistry, United States, 2016.

[55] YT Male, IW Sutapa, IB Kapelle and M Lopulalan. Qsar modeling and design of a new model of anti-hiv drug 1-aryl-tetrahydroisoquinoline derived using the PM3 semiempirical method. *Rasayan Journal of Chemistry* 2022; **15(1)**, 359-368.

[56] Z Yu, Y Duan, L Cheng, Z Han, Z Zheng, H Zhou, J Wu and Y Tian. Aggregation induced emission in the rotatable molecules: The essential role of molecular interaction. *Journal of Materials Chemistry* 2012; **22(33)**, 16927-16932.

[57] S Guieu, F Cardona, J Rocha and AMS Silva. Tunable color of aggregation-induced emission enhancement in a family of hydrogen-bonded azines and schiff bases samuel. *Chemistry - A European Journal* 2018; **24(65)**, 17262-17267.

[58] J-S Chen, P-W Zhou, L Zhao and T-S Chu. A DFT/TDDFT study of the excited state intramolecular proton transfer based sensing mechanism for the aqueous fluoride chemosensor BTTPB. *RSC Advances* 2014; **4(1)**, 254-259.

[59] YT Male, I Wayan Sutapa and OM Ranglalin. Computational study natural color essence (Dyes) as active material on organic solar cell with Density Functional Theory (DFT). *Indonesian Journal of Chemical Research* 2015; **2(2)**, 205-212.

[60] R Hadanu, S Idris and IW Sutapa. QSAR analysis of benzothiazole derivatives of antimalarial compounds based on AM1 semi-empirical method. *Indonesian Journal of Chemistry* 2015; **15(1)**, 86-92.

[61] R Hadanu, L Adelin and IW Sutapa. Qsar studies of nitrobenzothiazole derivatives as antimalarial agents. *Makara Journal of Science* 2018; **22(1)**,

35-41.

[62] IW Sutapa, R Armunanto and K Wijaya. EFFECT of scandium on hidrogen dissociation energy at magnesium surface: *Ab initio* dft study. *Indonesian Journal of Chemistry* 2010; **10(2)**, 184-188.

[63] PJ Hay and WR Wadt. *Ab initio* effective core potentials for molecular calculations. Potentials for K to Au including the outermost core orbitale. *The Journal of Chemical Physics* 1985; **82(1)**, 299-310.

[64] PJ Hay and WR Wadt. *Ab initio* effective core potentials for molecular calculations. Potentials for the transition metal atoms Sc to Hg. *The Journal of Chemical Physics* 1985; **82(1)**, 270-283.

[65] WR Wadt and PJ Hay. *Ab initio* effective core potentials for molecular calculations. Potentials for main group elements Na to Bi. *The Journal of Chemical Physics* 1985; **82(1)**, 284-298.

[66] S Khan, M Muhammad, HM Al-Saidi, AA Hassanian, W Alharbi and KH Alharbi. Synthesis, characterization and applications of schiff base chemosensor for determination of Cu^{2+} ions. *Journal of Saudi Chemical Society* 2022; **26(4)**, 101503.

[67] Y He, J Yin and G Wang. New selective "on-off" fluorescence chemosensor based on carbazole Schiff base for Fe^{3+} detection. *Chemistry of Heterocyclic Compounds* 2018; **54(2)**, 146-152.

[68] KC Tayade, AS Kuwar, UA Fegade, H Sharma, N Singh, UD Patil and SB Attarde. Design and synthesis of a pyridine based chemosensor: Highly selective fluorescent probe for Pb^{2+}. *Journal of Fluorescence* 2014; **24(1)**, 19-26.

[69] A Kumar, Virender, N Kumar, A Chauhan and B Mohan. A reversible Schiff base chemosensor for the spectroscopic and colorimetric sensing of Eu^{3+} ions in solution and solid-state. *Inorganica Chimica Acta* 2024; **560**, 121833.

[70] P Yadav, S Gond, A Singh and VP Singh. Development of a reversible chromogenic sensor for Cu^{2+} in aqueous ethanol. *Materials Letters* 2021; **295**, 129869.

[71] A Kumar, Virender, B Mohan, AA Solovev, M Saini and HK Sharma. Development of 2-hydroxy-naphthaldehyde functionalized Schiff base chemosensor for spectroscopic and colorimetric detection of Cu^{2+} and Pd^{2+} ions. *Microchemical Journal* 2022; **180**, 107561.

[72] T Zhong, X Wang, C Li, J Xiu, Y Chen and G Wang. A single fluorescent chemosensor for detecting Ag^{+} ion in DMF and common trivalent metal ions in ethanol. *Journal of Molecular Structure* 2023; **1294**, 136436.

[73] A Brouwer. Standards for photoluminescence quantum yield measurements in solution (IUPAC Technical Report)*. *Pure and Applied Chemistry* 2011; **83**, 2213-2228.

[74] MP Andersson and P Uvdal. New scale factors for harmonic vibrational frequencies using the B3LYP density functional method with the triple-ζ basis Set 6-311+G(d,p). *Journal of Physical Chemistry A* 2005; **109(12)**, 2937-2941.

[75] AA Benjamine, K Mawa, AL Laye, BA Lucie, K Soleymane, NB Robert, BEH Sawaliho and NY Thomas. Density functional theory (B3LYP/6-311+G(d, p)) study of stability, tautomerism and acidity of 2-Thioxanthine in gas and aqueous phases. *International Journal of Computational and Theoretical Chemistry* 2019; **7(1)**, 49.

[76] C Chiter, A Bouchama, T Nardjes, H Allal, M Yahiaoui, I Warad, A Zarrouk and A Djedouani. Synthesis, crystal structure, spectroscopic and hirshfeld surface analysis, NCI-RDG, DFT computations and antibacterial activity of new asymmetrical azines. *Journal of Molecular Structure* 2020; **1217**, 128376.

[77] J Al-Anshori, AF Abror, J Juliandri, A Safari and AT Hidayat. *In Silico* DFT (Density Functional Theory) study of chemosensor selectivity of 3-Oxo-3H-Benzo[f]chromen-2-Carboxylic acid (ABKK) on sodium metal ion using FMO (Frontier Molecular Orbital) analysis. *Jurnal Kimia Sains Dan Aplikasi* 2023; **26(8)**, 318-323.

[78] T Keawwangchai, N Morakot and B Wanno. Fluorescent sensors based on BODIPY derivatives for aluminium ion recognition: An experimental and theoretical study. *Journal of Molecular Modeling* 2013; **19(3)**, 1435-1444.

[79] M Mathivanan, B Tharmalingam, CH Lin, BV Pandiyan, V Thiagarajan and B Murugesapandian. ESIPT-active multi-color aggregation-induced emission features of triphenylamine–

salicylaldehyde-based unsymmetrical azine family. *CrystEngComm* 2019; **22(2)**, 213-228.

[80] PE Hansen and J Spanget-Larsen. NMR and IR investigations of strong intramolecular hydrogen bonds. *Molecules* 2017; **22(4)**, 552.

[81] P Charisiadis, VG Kontogianni, CG Tsiafoulis, AG Tzakos, M Siskos and IP Gerothanassis. 1H-NMR as a structural and analytical tool of intra- and intermolecular hydrogen bonds of phenol-containing natural products and model compounds. *Molecules* 2014; **19(9)**, 13643-13682.

[82] A Mohammadi and J Jabbari. Simple naked-eye colorimetric chemosensors based on Schiff-base for selective sensing of cyanide and fluoride ions. *Canadian Journal of Chemistry* 2016; **94(7)**, 631-636.

[83] S Kapoor, C Gopinathan, HS Mahal and RM Iyer. The fluorescence of tryptophan in N,N-dimethylformamide-water mixtures. *Chemical Physics Letters* 1989; **163(2)**, 135-139.

[84] T Mudalige, H Qu, D Van Haute, SM Ansar, A Paredes and T Ingle. Chapter 11 - Characterization of nanomaterials: Tools and Challenges. *Nanomaterials for Food Applications Micro and Nano Technologies* 2019; **1**, 313-353.

[85] M Tajbakhsh, GB Chalmardi, A Bekhradnia, R Hosseinzadeh, N Hasani and MA Amiri. A new fluorene-based Schiff-base as fluorescent chemosensor for selective detection of Cr^{3+} and Al^{3+}. *Spectrochimica Acta - Part A: Molecular and Biomolecular Spectroscopy* 2018; **189(15)**, 22-31.

[86] MJ Kamlet, JL M Abboud, MH Abraham and RW Taft. Linear solvation energy relationships. 23. A comprehensive collection of the solvatochromic parameters, π.*, α, and β, and some methods for simplifying the generalized solvatochromic equation. *The Journal of Organic Chemistry* 1983; **48(17)**, 2877-2887.

[87] VS Padalkar and S Seki. Excited-state intramolecular proton-transfer (ESIPT)-inspired solid state emitters. *Chemical Society Reviews* 2016; **45(1)**, 169-202.

[88] J Zhao, S Ji, Y Chen, H Guo and P Yang. Excited state intramolecular proton transfer (ESIPT): from principal photophysics to the development of new chromophores and applications in fluorescent molecular probes and luminescent materials. *Physical Chemistry Chemicsl Physics* 2012; **14**, 8803-8817.

[89] P Piyanuch, S Wangngae, A Kamkaew, W Wattanathana, S Wannapaiboon, S Impeng, W Maneeprakorn, V Promarak and K Chansaenpak. Ultrasensitive fluorogenic chemosensor based on ESIPT phenomenon for selective determination of Cu^{2+} ion in aqueous system and its application in environmental samples and biological imaging. *Dyes and Pigments* 2022; **205**, 110532.

[90] J Mei, NLC Leung, RTK Kwok, JWY Lam and BZ Tang. Aggregation-Induced emission : Together we shine , united we soar ! 2015; **115(21)**, 11718-11940.

[91] EM Santos, W Sheng, RE Salmani, ST Nick, A Ghanbarpour, H Gholami, C Vasileiou, JH Geiger and B Borhan. Design of large stokes shift fluorescent proteins based on excited state proton transfer of an engineered photobase. *Journal of the American Chemical Society* 2021; **143(37)**, 15091-15102.

[92] F Kaspar. Quality data from messy spectra: How isometric points increase information content in highly overlapping spectra. *ChemBioChem* 2023; **24(7)**, 202200744.

[93] B Pramanik and D Das. Aggregation-Induced emission or hydrolysis by water? The case of schiff bases in aqueous organic solvents. *The Journal of Physical Chemistry C* 2018; **122(6)**, 3655-3661.

[94] VS Padalkar and S Seki. Excited-state intramolecular proton-transfer (ESIPT)-inspired solid state emitters. *Chemical Society Reviews* 2016; **45(1)**, 169-202.

[95] KS Jagadhane, SR Bhosale, DB Gunjal, OS Nille, GB Kolekar, SS Kolekar, TD Dongale and PV Anbhule. Tetraphenylethene-based fluorescent chemosensor with mechanochromic and Aggregation-Induced Emission (AIE) properties for the selective and sensitive detection of Hg^{2+} and Ag^{+} ions in aqueous media: Application to environmental analysis. *ACS Omega* 2022; **7(39)**, 34888-34900.

[96] H Wang, L Da, L Yang, S Chu, F Yang, S Yu and C Jiang. Colorimetric fluorescent paper strip with smartphone platform for quantitative detection of cadmium ions in real samples. *Journal of*

Hazardous Materials 2020; **392**, 122506.

[97] A Samokhvalov. Analysis of various solid samples by synchronous fluorescence spectroscopy and related methods: A review. *Talanta* 2020; **216**, 120944.

[98] YK Zhang, N Wang, FT Wang, WF Zhou, YZ Zhang, M Yang, Z Li, L Geng, DS Zhang, S Zhuang and X Zhang. Solvent induced synthesis of fluorescence Zn(II)-based metal–organic frameworks with distinctive responsiveness to DMF stimuli. *Polyhedron* 2024; **258**, 117057.

[99] D Aydin. Sensing of aluminum and cyanide ions utilizing a novel bis-phenol a based fluorogenic probe: Applications in test stripts. *Microchemical Journal* 2020; **159**, 105477.

[100] J Cheng, Y Li, Z Zhu, H Guan, J Zhai, Y Xiang and M Wang. A simple and rapid "Turn-On" fluorescent probe based on binuclear schiff base for Zn^{2+} and its application in cell imaging and test strips. *Molecules* 2024; **29(24)**, 5850.

[101] X Liu, J Zhao and Y Zheng. Insight into the excited-state double proton transfer mechanisms of doxorubicin in acetonitrile solvent. *RSC Advances* 2017; **7(81)**, 51318-51323.

[102] B An, S Feng, K Wen, W Wu, H Yuan, Q Zhu, X Guo and J Zhang. Theoretical insights into the ultrafast excited-state intramolecular proton transfer (ESIPT) mechanism in a series of amide-based NH···N hydrogen-bonding compounds. *Organic Electronics* 2017; **45**, 1-8.

[103] G Yang, X Jin, K Chen and D Yang. Uncovering the excited state trends and ESIPT mechanism for 2-(hydroxy-3-dimethyl-phenyl)-benzooxazole-6-carboxylicacid. *Chemical Physics Letters* 2019; **736**, 136815.

[104] S Lee, J Lee and Y Pang. Excited state intramolecular proton transfer of 1,2-dihydroxyanthraquinone by femtosecond transient absorption spectroscopy. *Current Applied Physics* 2015; **15(11)**, 1492-1499.

[105] B Gierczyk, SS Murphree, MF Rode and G Burdzinski. Blockade of persistent colored isomer formation in photochromic 3H-naphthopyrans by excited-state intramolecular proton transfer. *Scientific Reports* 2022; **12**, 19159.

Supplementary materials

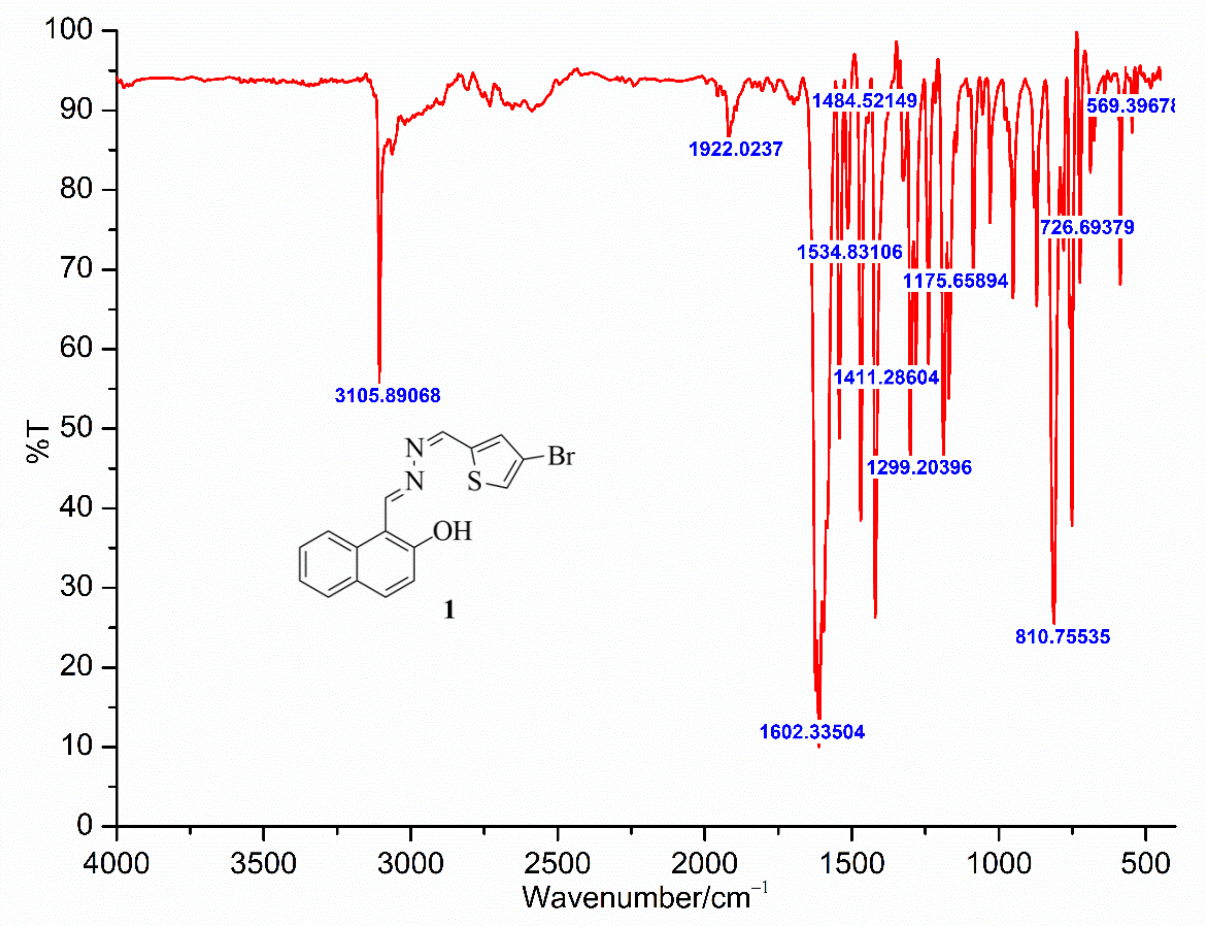

Figure S1 FTIR Spectra of **1** in KBr disk.

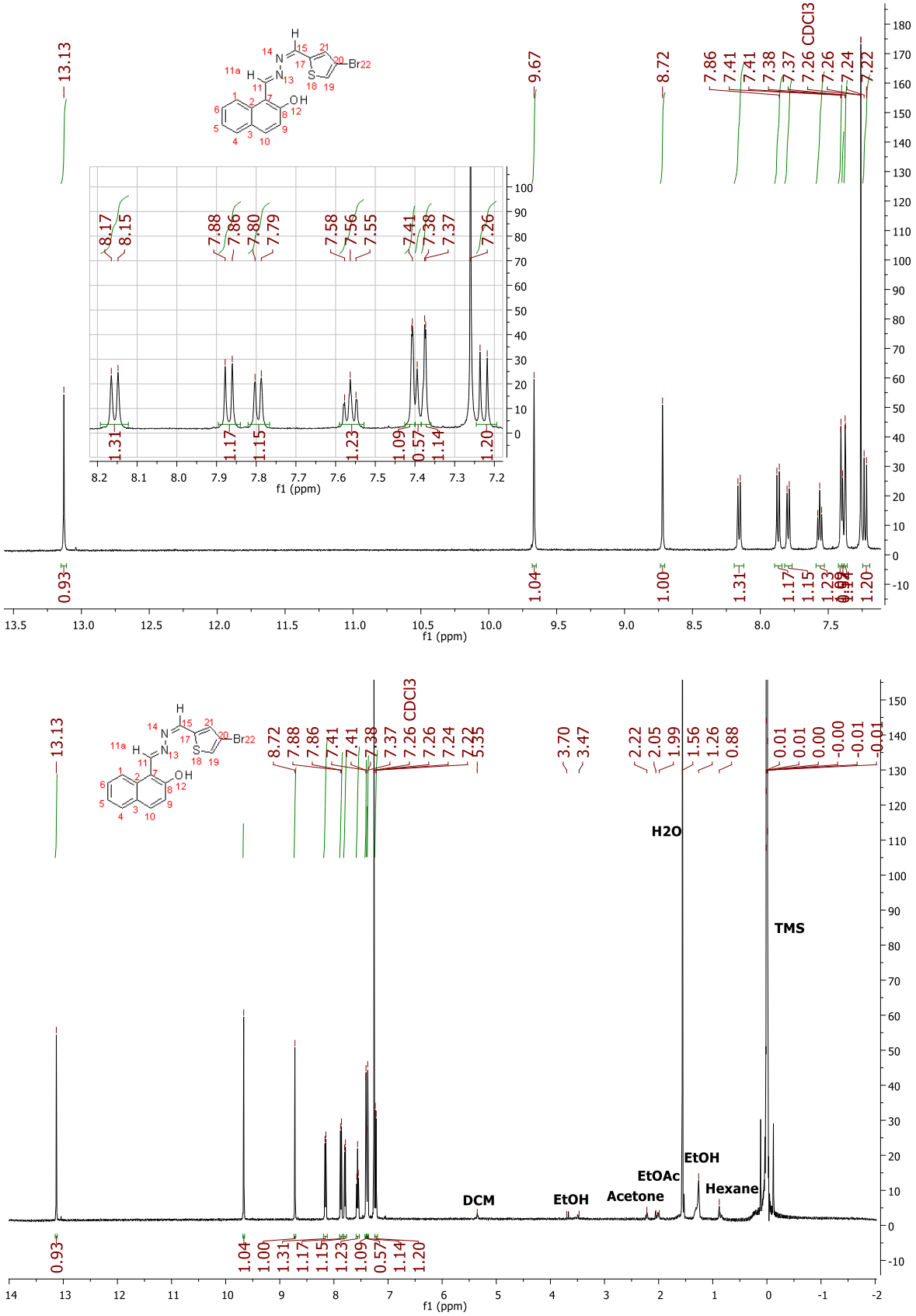

Figure S2 ^{1}H-NMR Spectra of **1** in $CDCl_3$ measured on Agilent 500 MHz NMR (Top: Zoom in, Bottom: Zoom out)

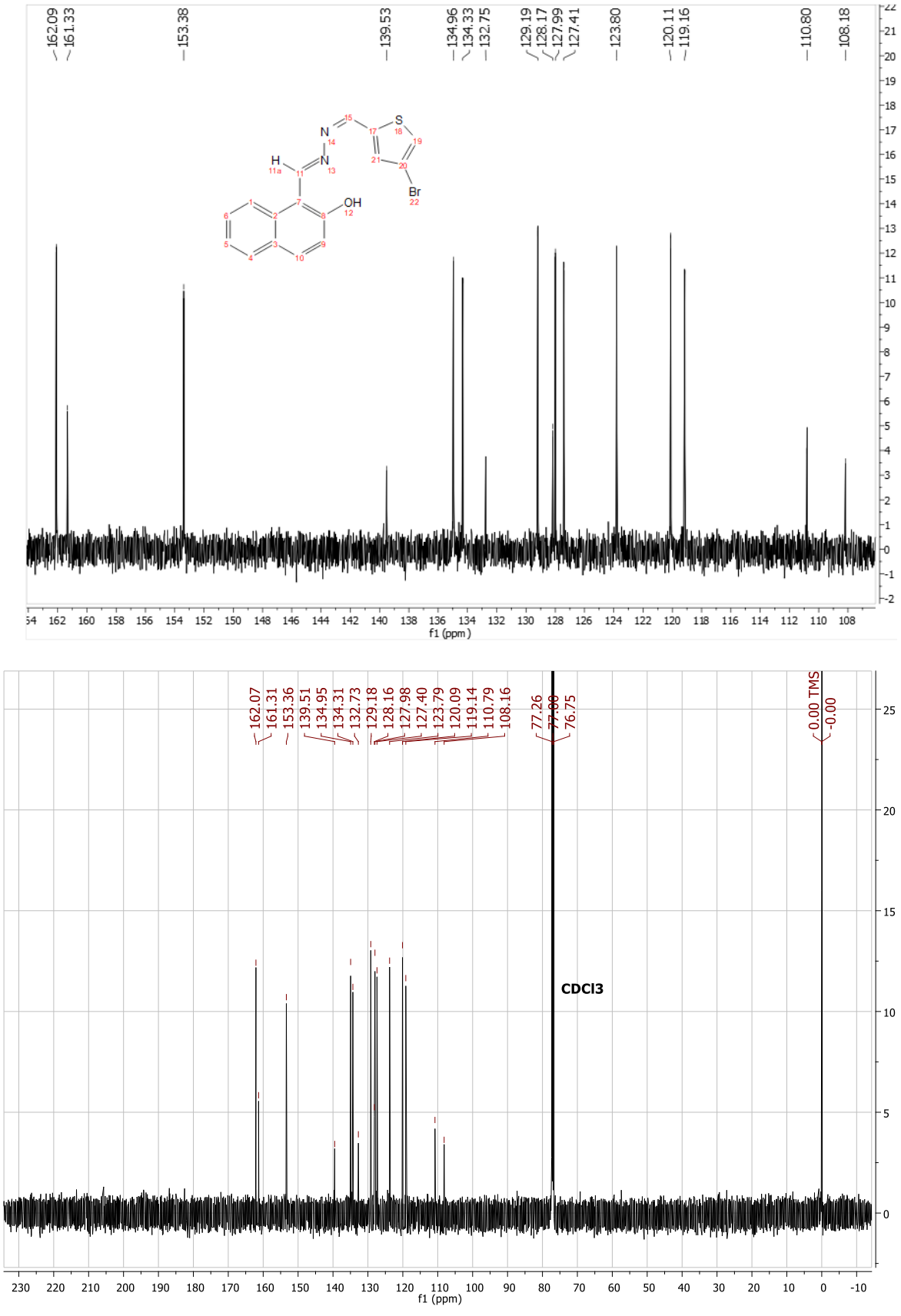

Figure S3 ^{13}C-NMR Spectra of **1** in $CDCl_3$ measured on Agilent 125 MHz NMR (Top: Zoom in, Bottom: Zoom out)

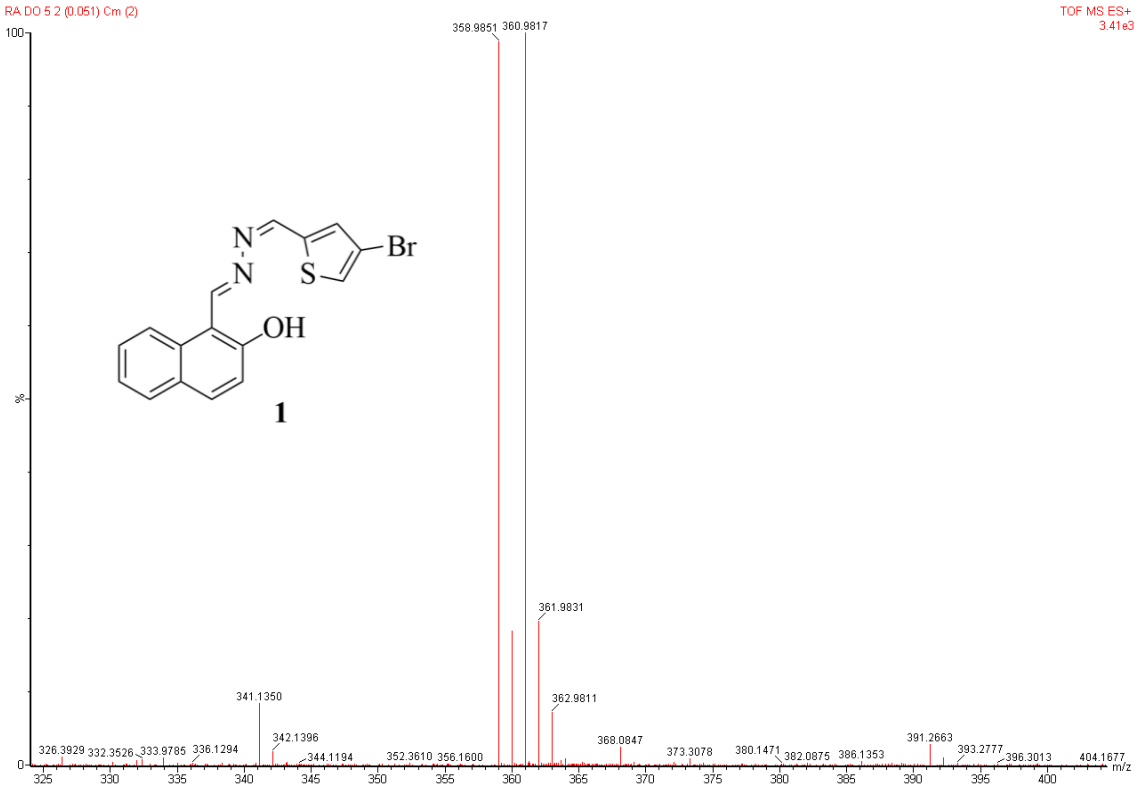

Figure S4 ToF-HRMS (ES^+) Spectra of compound **1**.

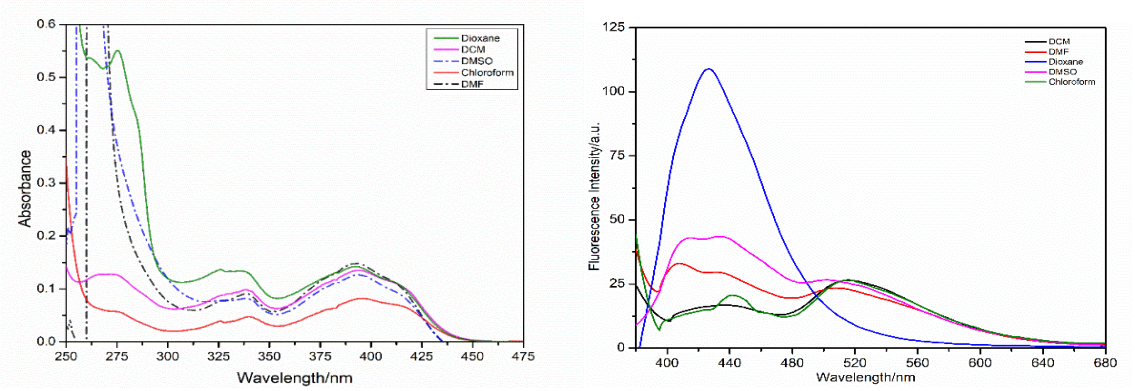

Figure S5 Absorption (Left) and emission (Right) spectra of **1** in various aprotic solvents (1.0 x 10^{-5} mole dm^{-3})

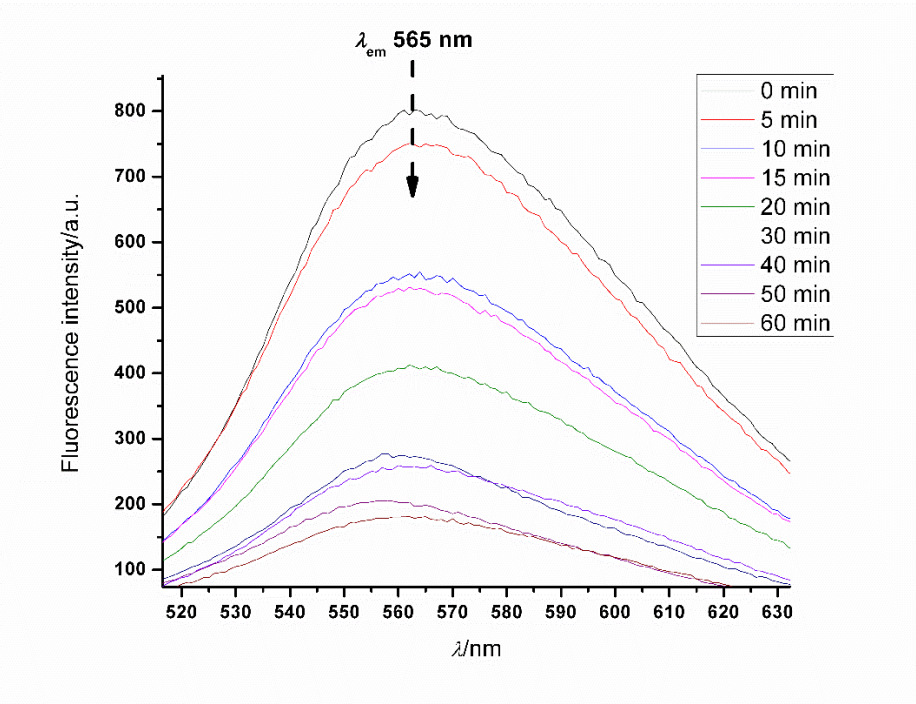

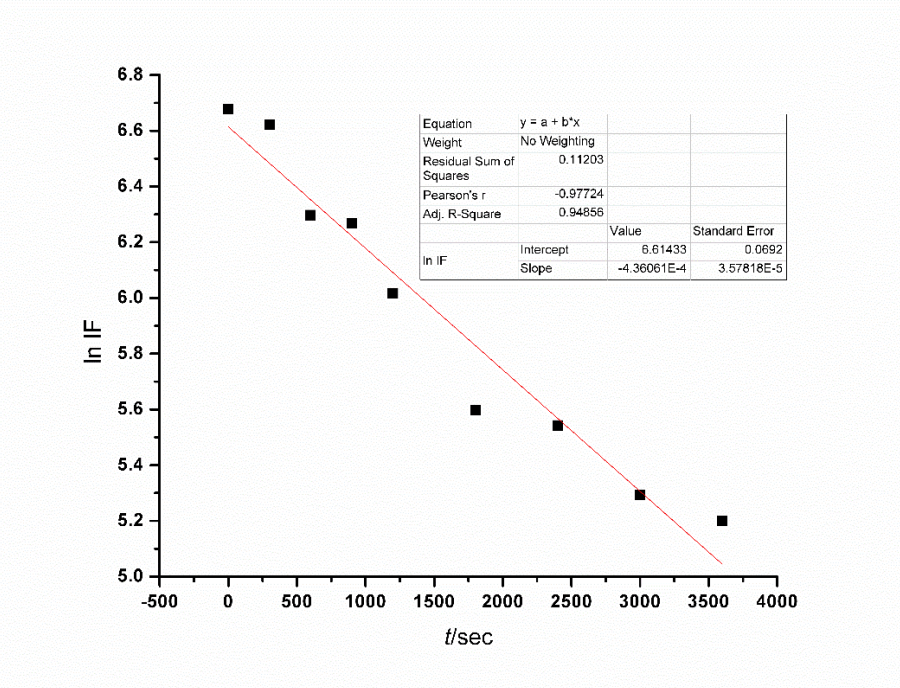

Slope	k	$t_{1/2}$=ln2/k (sec)	$t_{1/2}$ (min)
-0.0004	0.0004	1733	29

Figure S6 AIE stability test of **1** (1.0×10^{-4} mole dm^{-3}) DMF:H_2O (1:9, v/v) and their 1st order kinetic analysis at a stirred condition over time

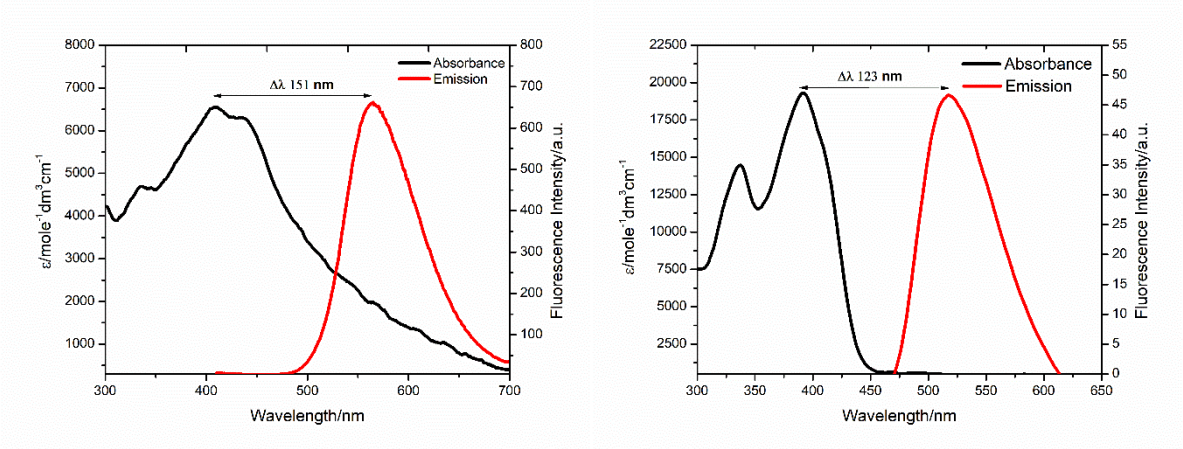

Figure S7 Absorption and Emission spectra of 1 in DMF:H_2O (1:9, *v*/*v*) (left) in DMF (right) and their Stokes Shift, λ_{ex} 360 nm

QS 1.0 x 10^{-9} mole dm^{-3} [1]	**1** 1.0 x 10^{-4} mole dm^{-3} [1]	**1**+Cu 1.0 x 10^{-4} mole dm^{-3} [1]
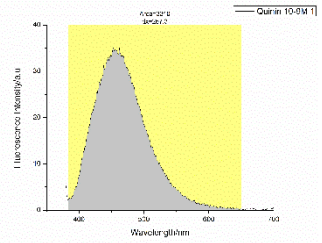	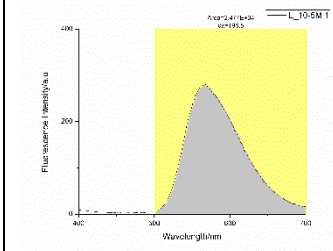	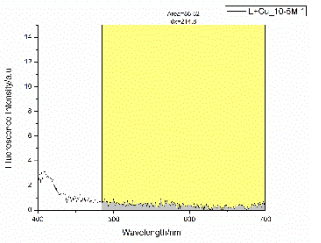
QS 1.0 x 10^{-9} mole dm^{-3} [2]	**1** 1.0 x 10^{-4} mole dm^{-3} [2]	**1**+Cu 1.0 x 10^{-4} mole dm^{-3} [2]
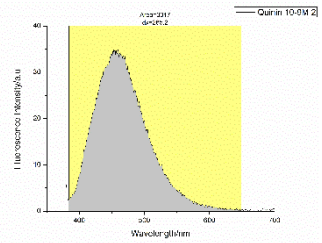	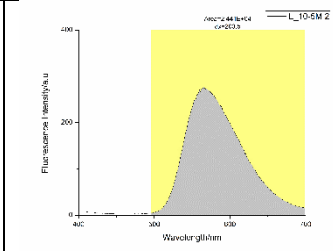	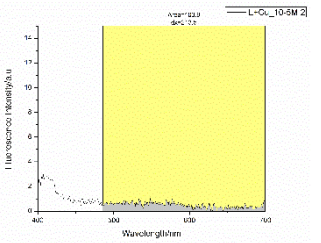
QS 1.0 x 10^{-9} mole dm^{-3} [3]	**1** 1.0 x 10^{-4} mole dm^{-3} [3]	**1**+Cu 1.0 x 10^{-4} mole dm^{-3} [3]
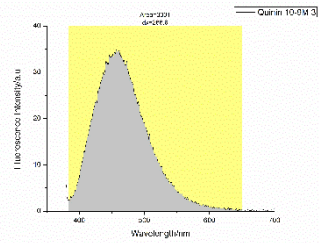	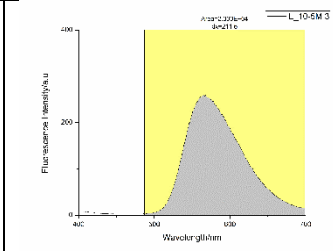	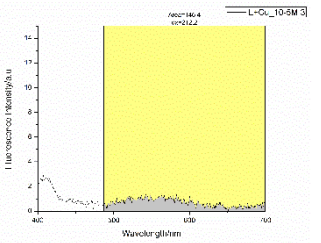
QS 1.0 x 10^{-9} mole dm^{-3} [4]	**1** 1.0 x 10^{-4} mole dm^{-3} [4]	**1**+Cu 1.0 x 10^{-4} mole dm^{-3} [4]
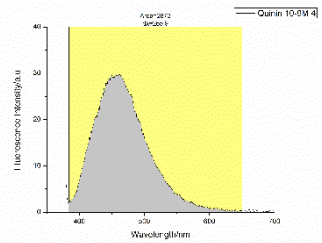	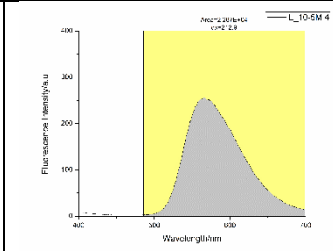	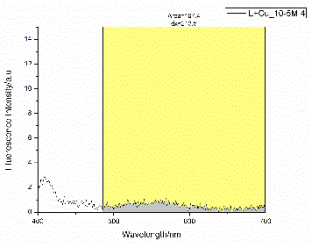
QS 1.0 x 10^{-9} mole dm^{-3} [5]	**1** 1.0 x 10^{-4} mole dm^{-3} [5]	**1**+Cu 1.0 x 10^{-4} mole dm^{-3} [5]
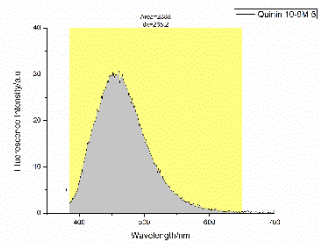	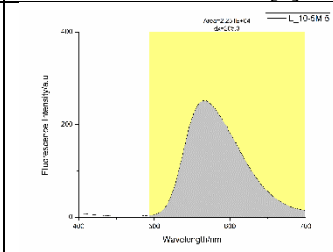	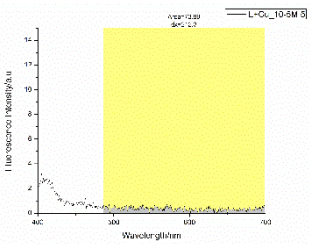

Figure S8 Integrated emission spectra of quinine sulfate (QS) standard (1.0 x 10^{-9} mole dm^{-3}), **1** (1.0 x 10^{-4} mole dm^{-3}), and 1+Cu^{2+} (1.0 x 10^{-4} mole dm^{-3}) for the quantum yield calculations.

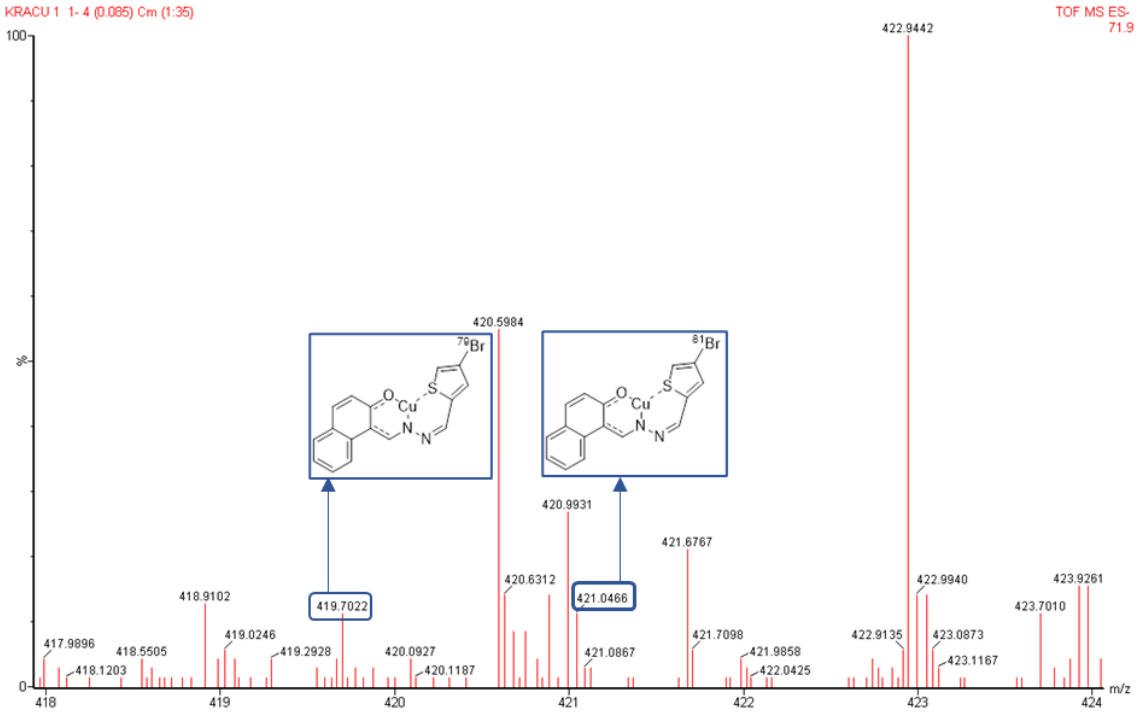

Figure S9 ToF-HRMS (ES⁻) Spectra of compound **1**+Cu^{2+} with their Br isotopic trace.

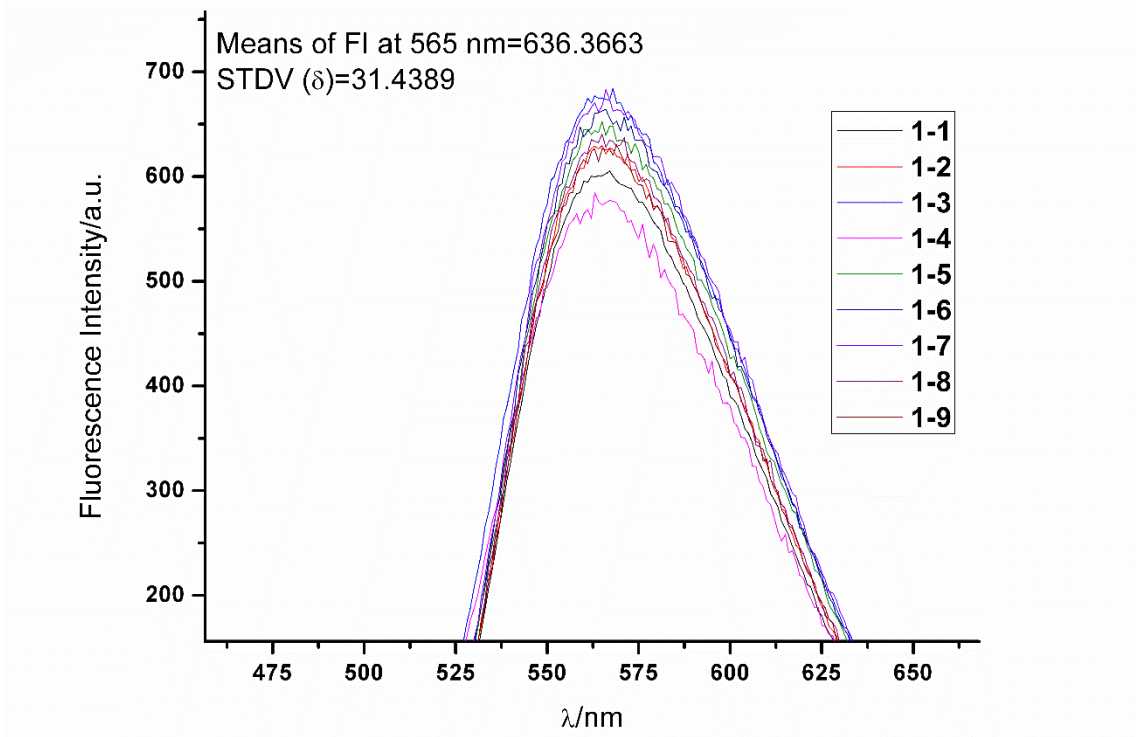

Figure S10 The emission spectra of **1** (1×10^{-4} mole dm^{-3} in DMF:H_2O (1:9, *v*/*v*)) and their means of fluorescence intensity (FI) at maxima with their standard deviation (δ).

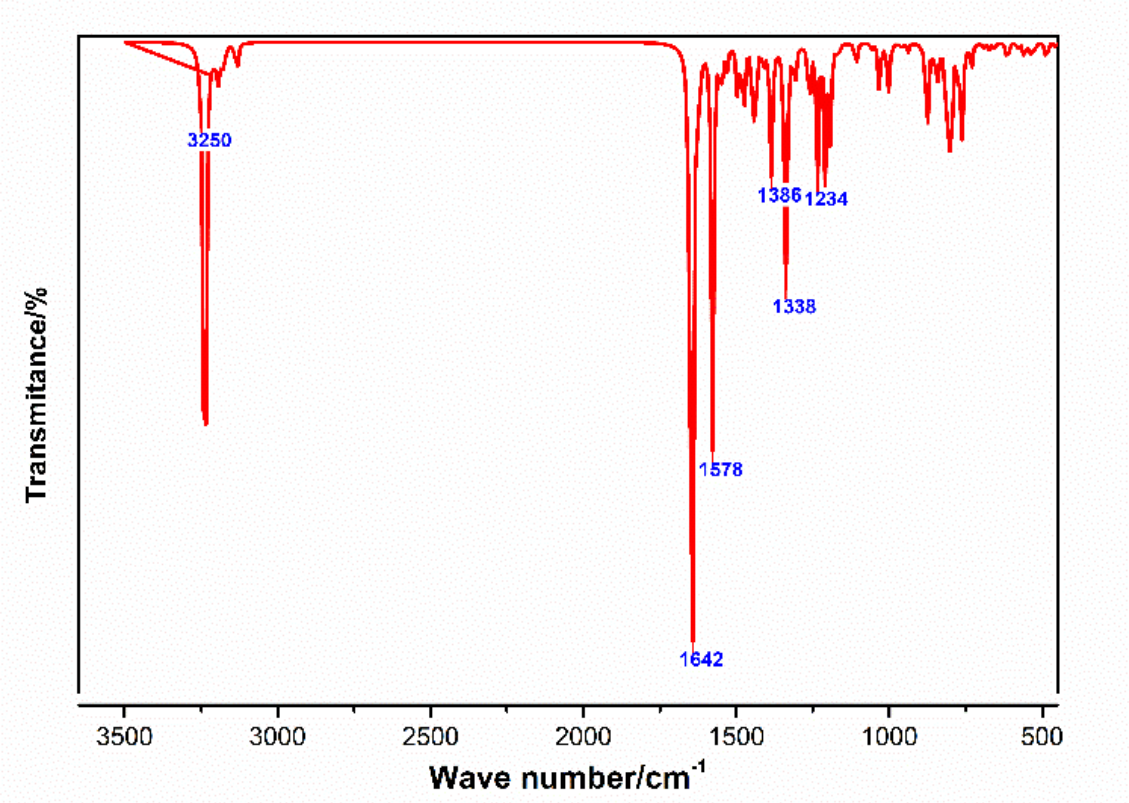

Figure S11 The calculated vibration frequencies of 1 at a minima state

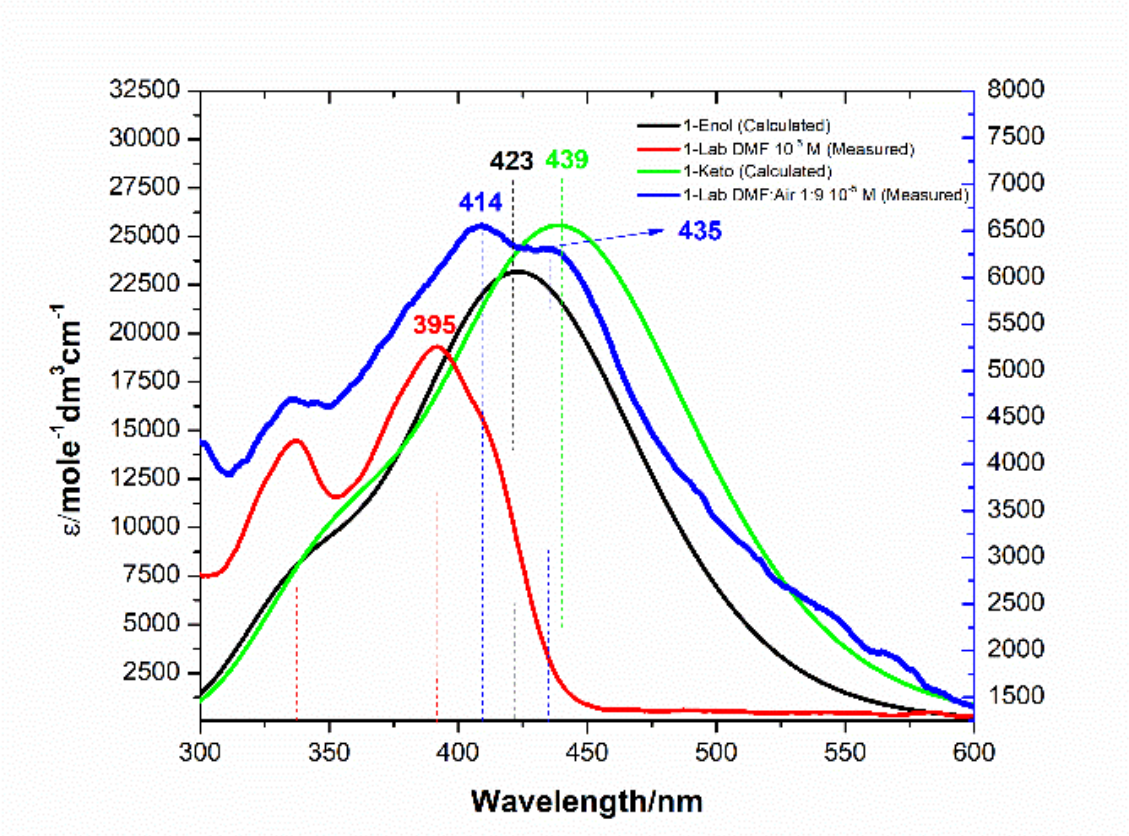

Figure S12 The calculated UV/Vis spectra of **1** at a minima state against the measured one in DMF and DMF:H_2O 1:9 *v*/*v*.

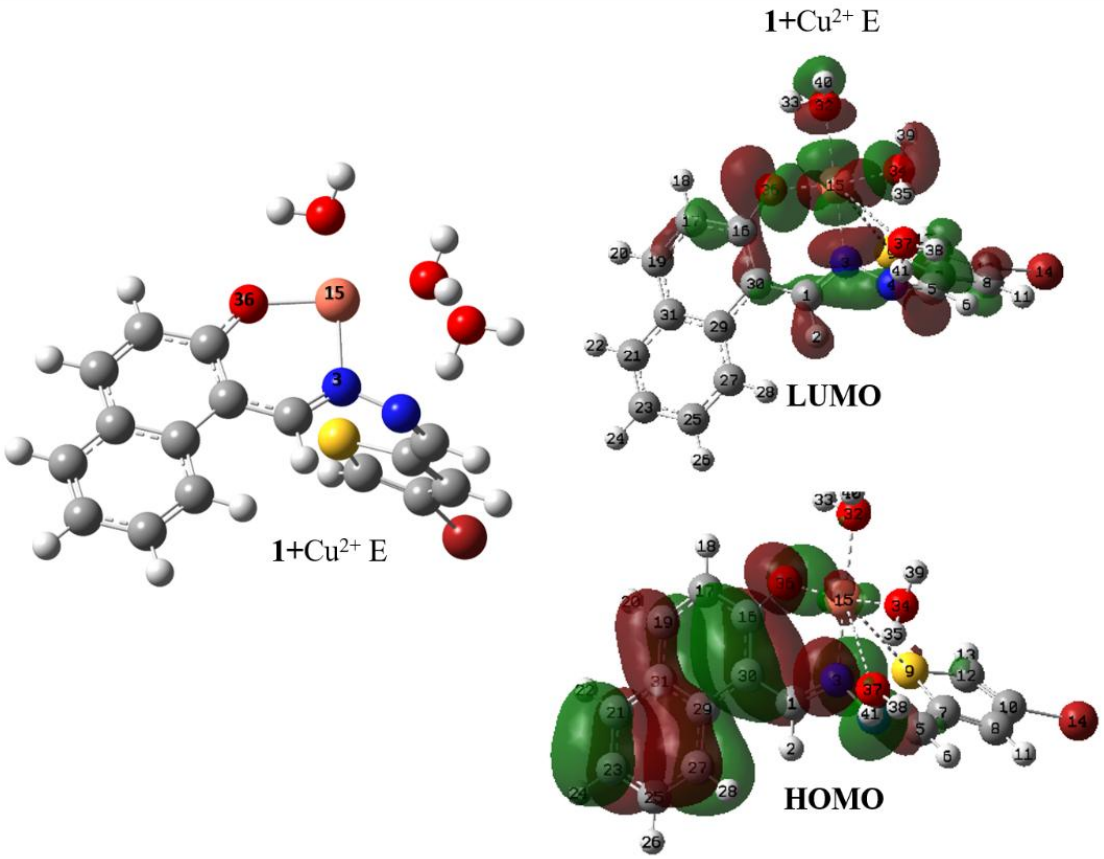

Figure S13 Optimized geometry structure of **1**+Cu^{2+} Enol at S_0 and its calculated frontier molecular orbital

Table S1 Calculated primary bond length (Å) and bond angle (°) of the optimized enol-keto of **1** at S_0 and S_1 state.

	1-Enol S_0		**1**-Keto S_0	
	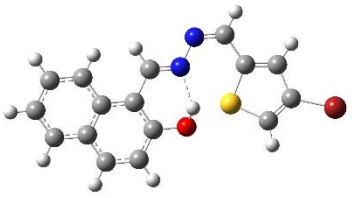		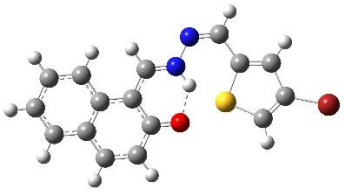	
	1-Enol S_1		**1**-Keto	S_1
	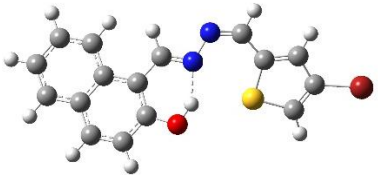		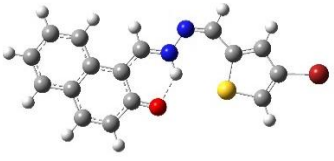	
	(S_0)	(S_1)	(S_0)	(S_1)
O_{19}-H_{20}	0.960	0.991	1.650	1.770
H_{20}-N_{21}	1.861	1.745	1.000	1.034
O_{19}-H_{20}-N_{21}	126.1°	146.2°	131.1°	133.3°

Table S2 The calculated frontier molecule orbital of **1**-Enol and **1**-Keto in DMF:H_2O

System		HOMO (eV)	LUMO (eV)	E gap (eV)	E_{total} (a.u.)	E_{total} (Kcal/mol)
1-Enol	DFT	-6.06	-2.68	3.38	-3773.59253487	-2367929,316
	TD-DFT	-6.06	-2.68	3.38	-3773.48543755	-2367862,112
1-Keto	DFT	-5.93	-2.72	3.21	-3773.58728973	-2367926,024
	TD-DFT	-5.93	-2.72	3.21	-3773.48438848	-2367861,454